D and D_s decay constants in $N_f = 2 + 1$ QCD with Wilson fermions

The RQCD collaboration and the ALPHA collaboration

Simon Kuberski [ID],[a,b,c] **Fabian Joswig** [ID],[d] **Sara Collins** [ID],[e] **Jochen Heitger** [ID][f] and **Wolfgang Söldner** [ID][e]

[a]*Theoretical Physics Department, CERN, 1211 Geneva 23, Switzerland*

[b]*Helmholtz-Institut Mainz, Johannes Gutenberg-Universität Mainz, Staudingerweg 18, 55128 Mainz, Germany.*

[c]*GSI Helmholtzzentrum für Schwerionenforschung, Planckstraße 1, 64291 Darmstadt, Germany*

[d]*Higgs Centre for Theoretical Physics, School of Physics and Astronomy, The University of Edinburgh, Edinburgh EH9 3FD, U.K.*

[e]*Institut für Theoretische Physik, Universität Regensburg, 93040 Regensburg, Germany.*

[f]*Institut für Theoretische Physik, Universität Münster, Wilhelm-Klemm-Straße 9, 48149 Münster, Germany*

E-mail: simon.kuberski@cern.ch, fabian.joswig@ed.ac.uk, sara.collins@ur.de, heitger@uni-muenster.de, wolfgang.soeldner@ur.de

ABSTRACT: We present results for the leptonic decay constants of the D and D_s mesons from $N_f = 2 + 1$ lattice QCD. We employ a set of 49 high statistics gauge ensembles generated by the Coordinated Lattice Simulations (CLS) effort utilising non-perturbatively improved Wilson fermions and the tree-level Symanzik improved gauge action at six values of the lattice spacing in the range $a = 0.098$ fm down to $a = 0.039$ fm, with pion masses varying from around 420 MeV down to below the physical point. The ensembles lie on three trajectories in the quark mass plane, two trajectories intersecting close to the physical quark mass point and the third one approaching the SU(3) chiral limit, enabling tight control of the light and strange quark mass dependence. We obtain $f_{D_s} = 246.8(1.3)$ MeV, $f_D = 208.4(1.5)$ MeV and $f_{D_s}/f_D = 1.1842(36)$, where the precision of our results is mostly limited by the determination of the scale.

Contents

1   Introduction

Flavour physics plays an important role in searches for signals of beyond the Standard Model interactions. In particular, non-unitarity of the Cabibbo-Kobayashi-Maskawa (CKM) matrix would be a strong indicator of new physics. Two elements of this CKM matrix, $|V_{cd}|$ and $|V_{cs}|$, can be deduced from the weak decays of D and D_s mesons into a lepton and a neutrino by combining experimentally measured decay rates with theory determinations of the decay constants f_D and f_{D_s}, respectively. Precise, ab-initio predictions of the decay constants are required and these can be obtained using lattice QCD. However, observables involving both charm and light or strange quarks are challenging to compute on the lattice with all sources of systematic uncertainty under control. The charm quark mass does not provide a high enough scale to admit an effective-field theory treatment, while employing a relativistic quark action with discretisation effects typically of $O(a^2)$, including $O(m_c^2 a^2)$, requires simulations with fine lattice spacings. Furthermore, the light (and strange) quark mass dependence needs to be sufficiently constrained, in particular, close to the physical point.

In this work we present results for the D and D_s decay constants from an analysis of $N_f = 2+1$ gauge field configurations generated by the Coordinated Lattice Simulations (CLS) consortium [1–3] with non-perturbatively O(a) improved Wilson quarks [4, 5] and the tree-level Symanzik-improved gauge action [6]. The charm quark is introduced as a quenched flavour, thus making our setup a partially quenched realisation of the four-flavour theory. As argued later, the impact of a missing charm quark in the sea is expected to be below our small total uncertainties.

A unique feature of this study is that both the continuum limit extrapolation and light and strange quark mass dependence is tightly constrained by the use of 49 high-statistics ensembles, which lie on three trajectories in the (sea) quark mass plane and which span a range of lattice spacings from $a \approx 0.10$ fm down to below $a \approx 0.04$ fm (a^2 varies by a factor of 6). Two of the trajectories meet at the physical point: along one trajectory the flavour average of the light and strange quark masses is held constant, and along the other the strange quark mass is fixed to approximately its physical value. The third trajectory runs towards the SU(3) chiral limit, with the light and strange quark masses set to be equal. Overall, the pion mass varies from $m_\pi \approx 420$ MeV down to 129 MeV, where for most ensembles the spatial extent L is large enough such that $m_\pi L \gtrsim 4$ and significant finite-volume effects are avoided. Lattice spacings as fine as 0.04 fm are achieved utilising open boundary conditions in time [7] to avoid the problem of topological freezing.

The pseudoscalar meson decay constants are defined through matrix elements of the axial vector current between pseudoscalar states and the vacuum. For Wilson fermions, the current is multiplicatively renormalised and, in order to achieve leading order O(a^2) discretisation effects, O(a) improved. For the latter, this includes evaluating terms to remove the leading quark mass-dependent cutoff effects. We remark that, because of the precision non-perturbative determination of the renormalisation factor of ref. [8] and the improvement coefficients of refs. [9, 10] employed in our analysis, renormalisation and improvement is not a significant source of uncertainty in our results.

With both the light and strange quark masses varying across the ensembles, we perform a simultaneous chiral and continuum extrapolation of f_D and f_{D_s} with all correlations taken into account. Any mistuning of the trajectories, where for a particular lattice spacing the relevant trajectory does not go through the physical point, can be corrected for using the chiral-continuum fit parameterisation. Our final results at the physical point read

$$
\begin{aligned}
f_{D_s} &= 246.8(0.64)_{\text{stat}}(0.61)_{\text{sys}}(0.95)_{\text{scale}}[1.3]\,\text{MeV}\,, \\
f_D &= 208.4(0.67)_{\text{stat}}(0.75)_{\text{sys}}(1.11)_{\text{scale}}[1.5]\,\text{MeV}\,, \\
f_{D_s}/f_D &= 1.1842(21)_{\text{stat}}(22)_{\text{sys}}(19)_{\text{scale}}[36]\,,
\end{aligned}
\tag{1.1}
$$

where the first error is statistical, the second systematic (arising from the parameterisation of the lattice spacing and quark mass dependence), the third component is due to the scale setting (taken from ref. [3]) and within the last bracket we give the total uncertainty. These results are the most precise for $N_f = 2+1$ lattice QCD to-date and are consistent with the recent work of ref. [11], which utilises a sub-set of the ensembles employed here (with a mixed action setup). Our errors are more than twice those quoted by FNAL/MILC in their $N_f = 2+1+1$ study [12] (see the 2021 FLAG report [13] for a comprehensive review

of lattice results). An immediate improvement in our results would be achieved through a more precise determination of the scale. However, once the uncertainties are reduced to the level of a few per mille, isospin-breaking effects, as well as the absence of charm sea quarks, will need to be considered.

The structure of the rest of the paper is as follows. In section 2 we give details of our lattice setup and the ensembles employed. The construction of the two-point correlation functions is discussed in section 3, along with the Symanzik improvement and renormalisation of the relevant heavy-light operators. The fitting procedure to extract the bare decay constants from the correlation functions is described in section 4. Finite-volume effects are not significant in our setup, and this is demonstrated in section 5. In section 6, we outline the set of chiral and continuum limit extrapolations performed and how the results at the physical point are combined via a model averaging procedure. We also specify our choice of hadronic scheme, i.e. the lattice scale employed and the external (physical) input used to define the physical quark masses. The final results are presented in section 7 and compared with previous works. We conclude in section 8. Additional information on the simulations, including the masses and bare decay constants for the individual ensembles and the scheme dependence of the final results, are collected in appendices. Preliminary accounts of this work have been presented in refs. [14, 15].

2 Lattice setup

In the following we describe the set of $N_{\mathrm{f}} = 2 + 1$ ensembles utilised in our analysis. We have employed non-perturbatively $\mathrm{O}(a)$ improved Wilson fermions [4, 5] and the tree-level Symanzik improved gauge action [6]. All ensembles have been created within the CLS effort.[1] We have ensembles at six values of the squared bare coupling constant $g_0^2 = 6/\beta$, which corresponds to lattice spacings ranging from $a = 0.098\,\mathrm{fm}$ down to $a = 0.039\,\mathrm{fm}$. At each value of β, simulations are carried out along three trajectories in the quark mass plane, as visualised in figure 1:

- The $\mathrm{Tr}M = \mathrm{const.}$ line: the trace of the (bare) quark mass matrix M is kept fixed, $\mathrm{Tr}M = 2m_{\mathrm{l}} + m_{\mathrm{s}} = \mathrm{const..}$ The latter also holds for the renormalised quark masses up to $\mathrm{O}(a)$ effects, $2\widehat{m}_{\mathrm{l}} + \widehat{m}_{\mathrm{s}} = \mathrm{const.} + \mathrm{O}(a)$. The constant is chosen such that the flavour average of the pseudoscalar octet meson masses squared rescaled with the Wilson flow parameter t_0 is close to its physical value, $\bar{\mathsf{M}}^2 \equiv 8t_0\left(2m_{\mathrm{K}}^2 + m_{\pi}^2\right)/3 = \bar{\mathsf{M}}_{\mathrm{phys}}^2$, where m_{π} and m_{K} are the masses of the pion and kaon, respectively. See refs. [3, 16] for more details on the simulations along this trajectory.

- The $\widehat{m}_{\mathrm{s}} \approx \mathrm{const}$ line: the renormalised strange quark mass is kept approximately constant. The constant is chosen such that $\widehat{m}_{\mathrm{s}}$ is near its physical value, $\widehat{m}_{\mathrm{s}} \approx \widehat{m}_{\mathrm{s}}^{\mathrm{phys}}$, see ref. [17] for further details.

---

[1]For uptodate information on the CLS $N_{\mathrm{f}} = 2 + 1$ ensembles, see https://www-zeuthen.desy.de/alpha/public-cls-nf21/.
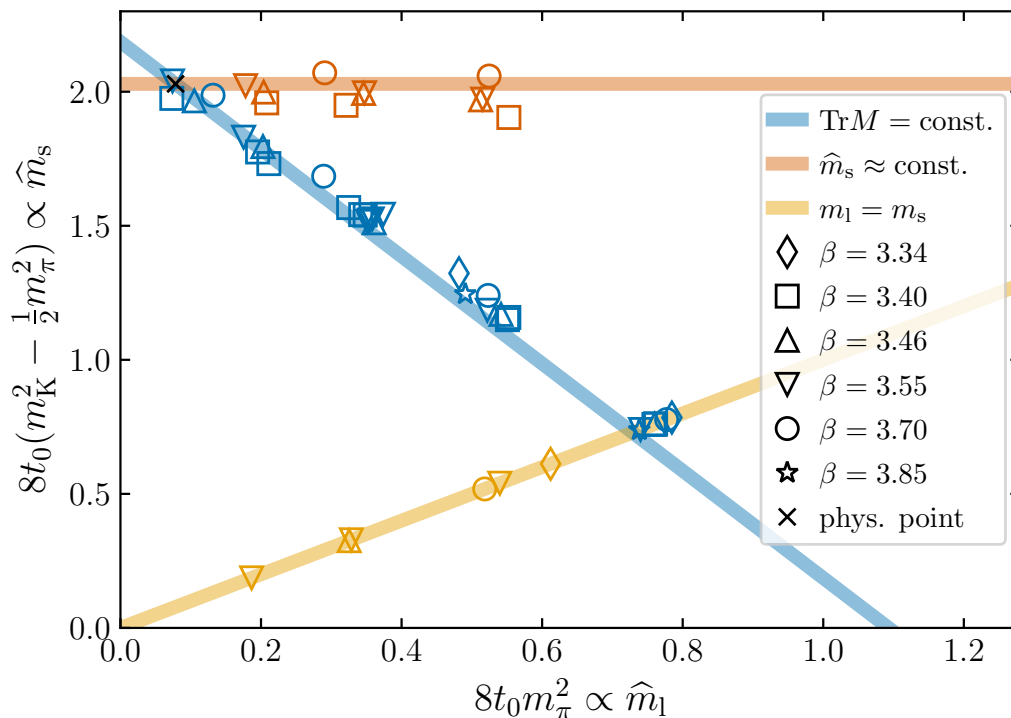
Figure 1. Overview of the ensembles used in this work in the plane of (renormalised) light and strange quark masses: the chiral trajectory where $\mathrm{Tr}M = \mathrm{const.}$ approaches the physical point from below (blue line) and meets the trajectory with renormalised strange quark mass $\widehat{m}_\mathrm{s} \approx \mathrm{const.}$ (orange line) at the physical point by construction. A third trajectory for which the light and strange quark masses are equal, $m_\mathrm{l} = m_\mathrm{s}$ (yellow line), approaches the SU(3) chiral limit. The orange line is obtained by setting $8t_0(m_\mathrm{K}^2 - \frac{1}{2}m_\pi^2)$ to its physical value, analogously the blue line is defined by fixing $\bar{\mathbb{M}}^2 \equiv 8t_0\left(2m_\mathrm{K}^2 + m_\pi^2\right)/3 = \bar{\mathbb{M}}_\mathrm{phys}^2$.

- The symmetric line: the light and strange quark masses are equal, $m_\mathrm{l} = m_\mathrm{s}$. This line has an intersection point with the $\mathrm{Tr}M = \mathrm{const.}$ trajectory (referred to as the SU(3) symmetric point) and approaches the SU(3) chiral limit.

Note that in the literature often only either the $\mathrm{Tr}M = \mathrm{const.}$ or the $\widehat{m}_\mathrm{s} \approx \mathrm{const}$ trajectory is considered when chiral extrapolations are performed. In such cases, (ideally) small deviations of the simulation points from the desired chiral trajectory arise due to discretisation effects and mistuning of the simulation parameters (as the simulation parameters that would match the desired trajectory can only be determined after the quark mass plane has been sufficiently explored). The latter deviations are often corrected by means of reweighting or a Taylor expansion [16]. The need to employ such methods is avoided in our analysis, since our set of ensembles allows for a reliable parametrisation of both the light and strange quark mass dependence of our observables and the extraction of the results at the physical point.

An overview of the lattice spacings and pion masses of the ensembles we utilise is shown in figure 2. More details are given in tables 2 and 3 in appendix A. In order to circumvent critical slowing down towards the continuum limit due to the freezing of the topological charge [18], open boundary conditions in time [7] have been implemented for ensembles with
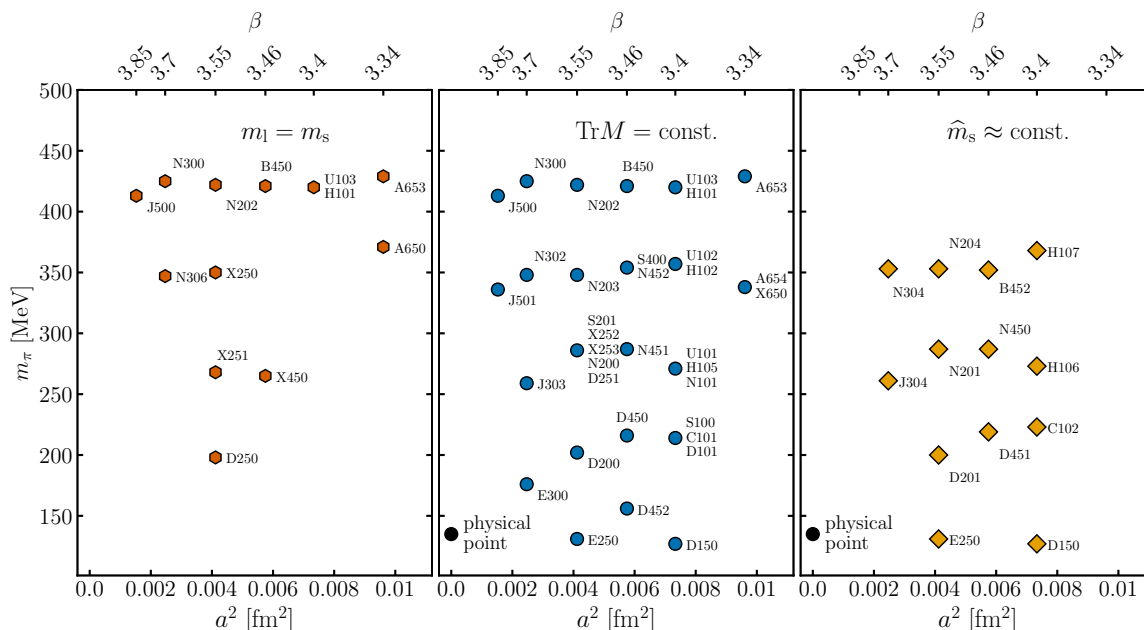
Figure 2. Overview of the ensembles entering the present study: three different quark mass trajectories (left: $m_l = m_s$, centre: $\mathrm{Tr}M = $ const., right: $\widehat{m}_s \approx$ const.) have been analysed at six (four for $\widehat{m}_s \approx$ const.) different lattice spacings. Additional ensembles with different spatial volumes exist for selected parameter sets. From these dedicated ensembles, the small volumes (S100, S201, U101, U102, U103, X252, X253) do not enter the final extrapolation. Also the ensembles B452 and N300 have been excluded. For these two cases the rather small temporal extent, in view of the given statistics, did not allow for a reliable extraction of the ground state.

$a \lesssim 0.05\,\mathrm{fm}$, while for other ensembles, antiperiodic boundary conditions have also been used. In the spatial directions, periodic boundary conditions are always imposed. We emphasise that for four of the six lattice spacings (the exceptions are the coarsest and finest lattice spacings) the ensembles provide excellent coverage of the quark mass plane in the region of interest. All together, this setup enables a detailed investigation of the quark mass and cutoff dependence when performing combined chiral-continuum extrapolations of the decay constants to the physical point.

The charm quark is partially quenched in our analysis. Two values of the charm quark mass are employed per ensemble, which are chosen such that only a small interpolation or (in a few cases) extrapolation to the physical value is required. The dependence of the charm quark mass on the light and strange sea quark masses is expected to be mild and we usually use the same hopping parameters for a given gauge coupling. The values of the hopping parameters for the light, strange and charm quarks are listed in table 3. The bare quark mass am_h of the heaviest quark, as defined in eq. (3.4), ranges from 0.48 on the coarsest ensembles to 0.14 on the finest ones.

Finite-size effects can also be quantified in our analysis. Ensembles were generated with different spatial extents at several simulation points for $m_\pi > 200\,\mathrm{MeV}$ and $a \geq 0.064\,\mathrm{fm}$. In particular, at $m_\pi \approx 286\,\mathrm{MeV}$ and $a = 0.064\,\mathrm{fm}$, five volumes are realised with $m_\pi L$ ranging from 3.0 to 5.9. As detailed in section 5, we find that finite volume effects are under control

for $m_\pi L \gtrsim 3.5$. We impose an additional cut of $L \geq 2.3\,\mathrm{fm}$ to ensure that the spatial extent is much larger than the inverse pseudo-critical temperature. We remark that for almost all simulation points there exists at least one ensemble with a spatial lattice extent $L \gtrsim 4/m_\pi$.

We achieve high statistics across our set of ensembles. In particular, for almost all ensembles we have a large number of configurations with respect to the (possibly) slowest mode in the simulation. See table 2 of appendix A for the number of configurations utilised for each ensemble and ref. [3] for details on the autocorrelations. The resulting precision of better than $0.6‰$ and $6‰$ for the heavy-light meson masses and bare decay constants, respectively, is illustrated in tables 4 and 5.

More details on the simulations performed by CLS using the OPENQCD code [19, 20] can be found in refs. [1–3]; we highlight here that the code package has several algorithmic improvements built in, such as the Hasenbusch trick [21], improved integrators [22], a multi-level integration scheme [23] and a deflated solver [24, 25]. Furthermore, for the $N_\mathrm{f} = 2$ light fermion part of the action, a twisted mass term is added in order to increase the stability of the HMC simulation [19, 26]. The effect of this additional term is removed by appropriate reweighting of the observables. Note that reweighting is also applied in the strange sector in order to account for errors arising from the use of a rational approximation [27, 28]. The strange quark reweighting factor usually does not vary significantly, however, it turns out that the factor can acquire a negative sign [29], which should be included in the ensemble averages. We utilise the signs calculated in refs. [26, 29] in our analysis. Only very few configurations have a negative strange reweighting factor and the effect of the negative signs is to (at most) slightly increase the statistical uncertainty.

3 Observables

The pseudoscalar decay constants f_D and $f_{\mathrm{D_s}}$ are defined via the matrix elements of the axial vector current between D and $\mathrm{D_s}$ meson states at momentum p and the vacuum, respectively,

$$\langle 0|A_\mu^\mathrm{lc}|\mathrm{D}(p)\rangle = \mathrm{i}f_\mathrm{D}p_\mu, \qquad \langle 0|A_\mu^\mathrm{sc}|\mathrm{D_s}(p)\rangle = \mathrm{i}f_{\mathrm{D_s}}p_\mu. \tag{3.1}$$

The axial vector current is given by $A_\mu^{qc}(x) = \bar{q}(x)\gamma_\mu\gamma_5 c(x)$ for quark flavours $q = \mathrm{l,s}$. In order to remove $\mathrm{O}(a)$ cutoff effects from the matrix elements, we construct an improved current

$$A_\mu^{qc,\mathrm{I}} = A_\mu^{qc} + ac_\mathrm{A}\frac{1}{2}\left(\partial_\mu + \partial_\mu^*\right)P^{qc}, \tag{3.2}$$

where the pseudoscalar operator is $P^{qc}(x) = \bar{q}(x)\gamma_5 c(x)$ and ∂_μ and ∂_μ^* denote the lattice forward and backward derivatives, respectively. Together with an $\mathrm{O}(a)$ improved fermion action, the above current eliminates all $\mathrm{O}(a)$ effects in the chiral limit. At non-vanishing quark mass, two additional terms are needed which depend on the valence quark masses and the sum of the sea quark masses. The renormalised $\mathrm{O}(a)$ improved current reads [30]

$$\left(A_\mu^{qc,\mathrm{I}}\right)_\mathrm{R} = Z_\mathrm{A}\left[1 + a\left(b_\mathrm{A}m_{qc} + \bar{b}_\mathrm{A}\mathrm{Tr}M\right)\right]A_\mu^{qc,\mathrm{I}} + \mathrm{O}(a^2), \tag{3.3}$$

where m_{qc} and $\mathrm{Tr}M$ denote the bare vector Ward identity quark mass combinations

$$m_{qc} = \frac{1}{2}\left(m_q + m_c\right), \quad \mathrm{Tr}M = 2m_\mathrm{l} + m_\mathrm{s}, \quad \text{with } m_q = \frac{1}{2a}\left(\frac{1}{\kappa_q} - \frac{1}{\kappa_\mathrm{crit}}\right). \tag{3.4}$$

The hopping parameter for quark flavour q is denoted by κ_q and κ_{crit} labels its critical value. For the renormalisation factor Z_A and the improvement coefficients c_A and b_A, we employ the non-perturbative determinations of refs. [8–10], respectively. The improvement coefficient $\bar{b}_A$ has been computed in refs. [10, 31], however, as the coefficient is compatible with zero for the range of gauge couplings considered here, we set $\bar{b}_A = 0$ in our analysis. For κ_{crit} we utilise the results of ref. [3]. For convenience, we collect the values for the renormalisation factor, improvement coefficients and κ_{crit} for each gauge coupling used in this work in table 6 of appendix A.

We remark that the gauge coupling g_0^2 also undergoes O(a) improvement, $\tilde{g}_0^2 = g_0^2(1 + \frac{1}{3}ab_g(g_0^2)\mathrm{Tr}M)$, where to consistently apply Symanzik improvement to this order, the improved coupling should be held constant away from the chiral limit [30, 32]. While there has been a recent effort to calculate b_g non-perturbatively [33], there is no determination available as yet for the range of coupling constants relevant for our calculations and the simulations are performed at fixed values of g_0. Note that the renormalisation factor and coefficients of the mass-dependent improvement terms in eq. (3.3) should be evaluated at $\tilde{g}_0^2$. However, for the latter the difference between, for instance, b_A evaluated at g_0^2 or $\tilde{g}_0^2$ enters at O(a^2) and can be ignored. To leading order in perturbation theory $b_g(g_0^2) = 0.036g_0^2 + \mathrm{O}(g_0^4)$ [34]. Using this estimate, the values of the improved coupling associated with our ensembles are very close to g_0^2 and in practice we evaluate renormalisation factors (as well as the improvement coefficients) at the gauge coupling where we have actually performed the simulation.

Holding g_0^2 (and not $\tilde{g}_0^2$) fixed in the simulations, means that the lattice spacing depends (mildly) on the quark masses, $a = a(g_0^2, a\mathrm{Tr}M)$. This introduces (mass-dependent) cutoff effects of O(a) in dimensionful quantities extracted in the simulation (at fixed g_0^2), such as a meson mass am_{M}. This effect is also expected to be small. Nevertheless, we circumvent this issue by rescaling all dimensionful quantities with appropriate powers of the gradient flow parameter t_0 (determined on the same ensemble) to form dimensionless combinations such that the O(a) effects cancel.

In order to obtain the matrix elements of eq. (3.1), we evaluate the two-point functions

$$C_{A_0\tilde{P}}^{qc}(t) \equiv C_{A_0\tilde{P}}^{qc}(x_0, y_0) = -\frac{a^6}{L^3}\sum_{\vec{x},\vec{y}}\left\langle A_0^{qc,\mathrm{I}}(x)\left(\tilde{P}^{qc}(y)\right)^\dagger\right\rangle,$$

$$C_{\tilde{P}\tilde{P}}^{qc}(t) \equiv C_{\tilde{P}\tilde{P}}^{qc}(x_0, y_0) = -\frac{a^6}{L^3}\sum_{\vec{x},\vec{y}}\left\langle \tilde{P}^{qc}(x)(\tilde{P}^{qc}(y))^\dagger\right\rangle, \tag{3.5}$$

at zero momentum, where $t = x_0 - y_0$ is the difference between the sink and source timeslices, x_0 and y_0, respectively. The spatial extent is denoted by L. The correlators are calculated by means of point-to-all propagators, where, for the pseudoscalar interpolator at the source and sink $\tilde{P}^{qc(\dagger)}$, we apply Wuppertal smearing [35, 36] with APE-smoothed links [37]. The number of smearing iterations is varied across the ensembles to optimise the overlap with the ground state. More iterations are needed as the light quark mass decreases and we rescale the number of iterations with a^{-2} to ensure (roughly) the same root mean square quark smearing radius as the lattice spacing is varied. In table 2 of appendix A, the individual numbers of smearing iterations for each quark are summarised for all ensembles. For more details related to the smearing, we refer the reader to ref. [3].

We compute the above two-point functions for two charm quark masses close to the physical charm quark mass. For a given gauge coupling, the same two values of the hopping parameter are normally utilised for each ensemble and the number of smearing iterations employed for the charm quark is also kept fixed. Note that the charm propagators are computed with the highest numerical precision that is possible with our code: we impose relative residuals of around 10^{-15}. No problems due to the numerical accuracy of the charm quark propagators are observed when fitting to the correlation functions to extract the heavy-light meson masses and decay constants (within the fit ranges chosen). Our fitting procedure is outlined in the following section.

In order to increase statistics, source operators are inserted at different temporal positions. For ensembles with open boundaries, the source positions are placed on a fixed set of time slices (equally distributed within the bulk region, with random spatial positions), while for those with periodic boundaries, the source positions are chosen randomly for each configuration. The total number of sources (per configuration) for each ensemble can be found in table 2.

4 Extraction of the bare quantities

In this section we describe how we extract the masses and decay constants of the heavy-light and heavy-strange mesons from fits to the relevant two-point correlation functions. In the first step, we average the two-point functions over the source positions. While this is straightforward on ensembles with periodic boundary conditions, care has to be taken when open boundaries in the time direction are imposed as the data can only be averaged in the bulk of the lattice, where boundary effects are negligible and translational invariance is effectively restored. We identify the boundary region by fitting the $\tilde{P}\tilde{P}$ correlation function to the form suggested in ref. [19], which accounts for states which propagate in from the boundary, and by applying the criterion that the contribution of these states is less than $\frac{1}{4}$ of the statistical uncertainty of the correlation function. To be conservative, a minimal distance of $1.5\,\mathrm{fm}$ is taken, even when boundary states have decayed earlier. For the heavy-light mesons, this is the case for almost all ensembles. We then average over all two-point functions where the source and sink are in the bulk region. The resulting correlation function is free from significant boundary effects and only depends on the source-sink separation, although contributions from excited states are still present.

We take a similar approach when extracting the ground state masses and matrix elements of interest. We determine the region where excited state contamination has fallen below the noise by fitting the effective mass of each correlation function with the two-state functional form,[2]

$$m_{\mathrm{eff}}(t) = m_0 + c_1 \exp(-m_1 t)\,, \tag{4.1}$$

over the range $[t_{\mathrm{min}}, t_{\mathrm{max}}]$ and using the criterion from above. The upper end of the fit region t_{max} is set by the time slice where the relative statistical uncertainty of the effective mass

---

[2]We define the effective mass of a correlation function $C(t)$ by $m_{\mathrm{eff}}(t) = \log[C(t-a)/C(t+a)]/(2a)$ in the case of open boundary conditions, and in the case of periodic boundary conditions as the solution of $C(t)/C(t+1) = \cosh[m_{\mathrm{eff}}(t) \cdot (t-T/2)]/\cosh[m_{\mathrm{eff}}(t) \cdot (t+1-T/2)]$.
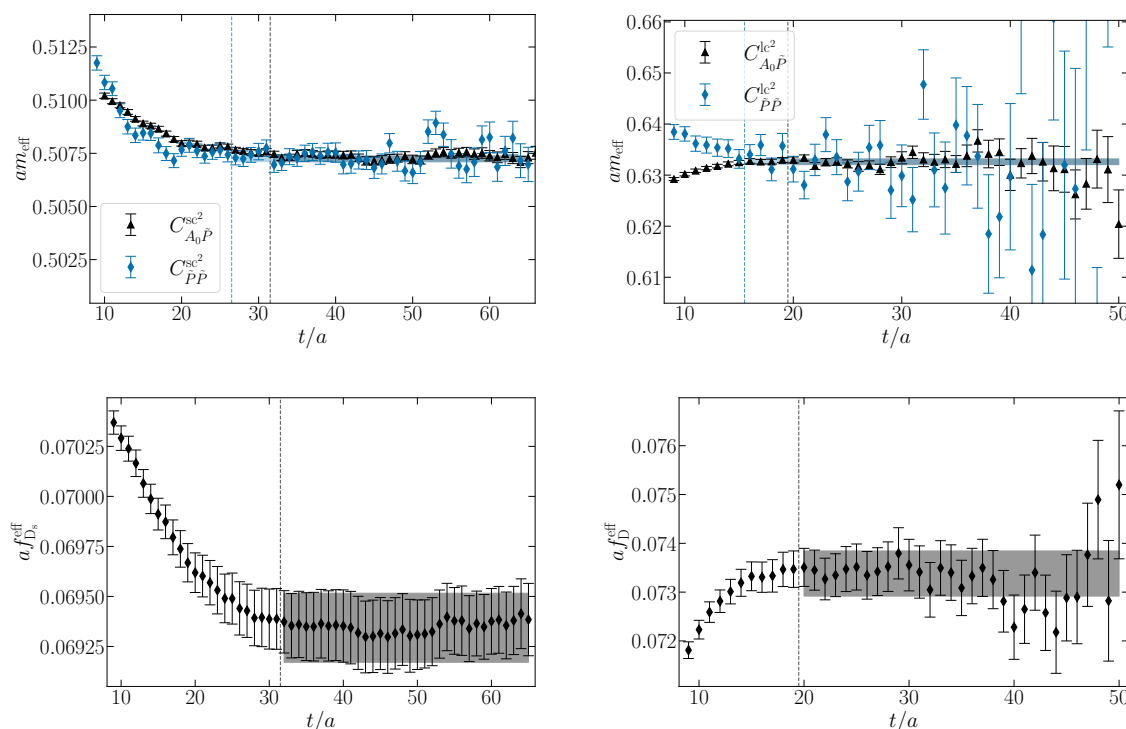
Figure 3. Results from our combined fits to the $\tilde{P}\tilde{P}$ and $A_0\tilde{P}$ two-point functions for the heavy-strange meson on ensemble E300 (left, $m_\pi = 175\,\text{MeV}$, $a = 0.049\,\text{fm}$) and the heavy-light meson on ensemble E250 (right, $m_\pi = 130\,\text{MeV}$, $a = 0.064\,\text{fm}$). Note that the results displayed are for the second charm hopping parameter (κ_{c^2}), see table 3 in appendix A. *Top:* the fit result for the meson mass $m_{D_{(s)}}$ (blue band) is shown together with the effective masses of the two correlation functions. The lower end of the fit range (t_{min}) in each case is indicated by a dashed line. *Bottom:* the result for the decay constant obtained from the fit (grey band) is displayed along with the effective decay constant (eq. (4.4)). The dashed line indicates the t_{min} of the $A_0\tilde{P}$ two-point function.

exceeds 8%. To fix the start of the fit region t_{min}, we scan over various fits, increasing t_{min} while keeping t_{max} fixed. The best fit is identified by monitoring the fit quality, as given by the reduced χ^2 for uncorrelated fits introduced in ref. [38]. To avoid overfitting in a region where only a single state can be resolved, we then identify the best fit to be the one with the highest Akaike weight, computed as outlined in section 6.4. In general, we find the determination of the region of ground state dominance to be largely insensitive to the procedure used to choose the best fit. The resulting regions of ground state dominance start in the range from 0.6 fm to 1.6 fm, where the variation within this range depends on the quark masses and the smearing parameters, as well as on the statistical accuracy of the data.

In the next step, we perform a combined fit to the $\tilde{P}\tilde{P}$ and $A_0\tilde{P}$ correlation functions within the fit ranges determined above. Excited state contributions can be neglected and the correlation functions as defined in eq. (3.5) are modelled with single-exponentials with the same energy m_D for $q = l$, and m_{D_s} for $q = s$ and amplitudes $A^{qc}_{A_0\tilde{P}}$ and $A^{qc}_{\tilde{P}\tilde{P}}$,

$$C^{qc}_{A_0\tilde{P}}(t) = A^{qc}_{A_0\tilde{P}}\,\mathrm{e}^{-m_{D_{(s)}}t}, \qquad C^{qc}_{\tilde{P}\tilde{P}}(t) = A^{qc}_{\tilde{P}\tilde{P}}\,\mathrm{e}^{-m_{D_{(s)}}t}. \tag{4.2}$$

Note that the $A_0\tilde{P}$ correlation function is constructed using the improved axial vector current in eq. (3.2). The combined fit helps to reduce the statistical uncertainty of the smeared-smeared $\tilde{P}\tilde{P}$ amplitude that is inherently noisier. Based on the spectral decomposition of the correlators, the bare matrix elements are extracted from the ground state energy and amplitudes via

$$f_{D_{(s)}} = \frac{\sqrt{2}A^{qc}_{A_0\tilde{P}}}{\sqrt{A^{qc}_{\tilde{P}\tilde{P}}m_{D_{(s)}}}} \, . \tag{4.3}$$

The renormalisation and remaining (mass-dependent) O(a) improvement are applied as outlined in section 6.2.

Representative results of the combined fits are displayed in figure 3. In the upper panels the fitted masses of the heavy-strange meson on ensemble E300 ($a = 0.05\,\mathrm{fm}$, $m_\mathrm{K} = 496\,\mathrm{MeV}$) and the heavy-light meson on ensemble E250 ($a = 0.064\,\mathrm{fm}$, $m_\pi \approx m_\pi^\mathrm{phys}$), are shown together with the effective masses of the corresponding $\tilde{P}\tilde{P}$ and $A_0\tilde{P}$ correlators. One can clearly see that the extraction of the mass is mostly constrained by the smeared-point two-point function. Thanks to the smearing of the pseudoscalar interpolator at the source, we can easily identify a region where excited state contributions are sufficiently suppressed. The lower panels compare the results for the decay constant, computed as given in eq. (4.3), with an effective decay constant constructed from the correlation functions and the fitted meson mass

$$f^{\mathrm{eff}}_{D_{(s)}}(t) = \frac{\sqrt{2}C^{qc}_{A_0\tilde{P}}(t)}{\sqrt{C^{qc}_{\tilde{P}\tilde{P}}(t)m_{D_{(s)}}\exp(-m_{D_{(s)}}t)}} \, . \tag{4.4}$$

These figures demonstrate that there are no significant excited state contributions present in the region, where we extract the meson masses and decay constants. For completeness, the analogous results for the heavy-light meson for ensemble E300 and the heavy-strange meson for ensemble E250 are displayed in figure 11 in appendix B.

We collect our results for the bare decay constants from O(a) improved currents for both choices of the heavy quark mass, enclosing the physical charm for almost all ensembles, in table 5 of appendix A. We find a statistical precision at the level of about 0.5% in most cases. The statistical uncertainties and the (auto-)correlations of the Monte Carlo data are determined and propagated using the Γ-method [39, 40]. We utilise the `pyerrors` package implementation of this method [41]. An analysis using the bootstrap method has also been performed as a consistency check. For the simultaneous interpolation to the physical point and extrapolation to the continuum limit, detailed in section 6, the masses of the light-light, light-strange and heavy-heavy mesons are also needed along with the flow scale t_0. The meson masses are extracted adopting the same procedure as outlined above. However, for the determination of the boundary for the pion, the smeared-source local-sink correlation function has been used (instead of the $\tilde{P}\tilde{P}$ correlation function), which for this particular case leads to a more conservative result. Table 4 in appendix A lists the meson masses and t_0 in lattice units obtained on each ensemble. Note that, in addition to the ensembles with small volumes discussed in the next section, ensembles B452 and N300 have been also excluded. For these two ensembles, the rather small temporal extent in view of the given statistics did not allow for a reliable extraction of the ground state.
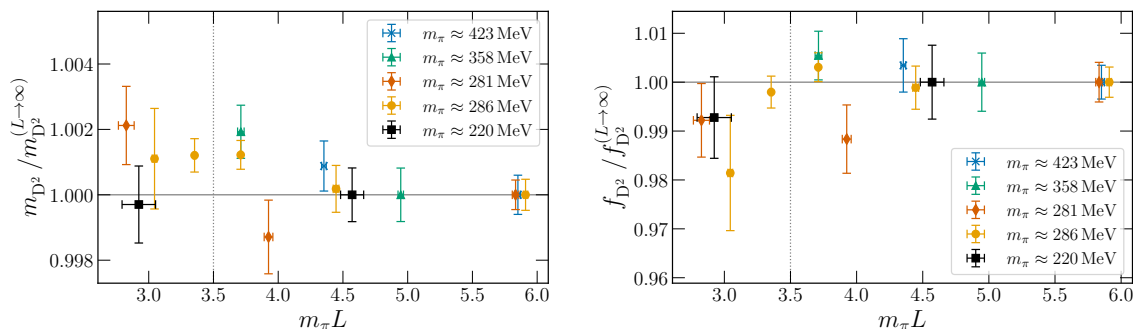
Figure 4. Volume dependence of the heavy-light meson mass (left) and decay constant (right). Results for fixed gauge coupling and light and strange quark masses but different spatial extents are normalised to the value on the ensemble with the largest spatial volume. Ensembles with $m_\pi L < 3.5$ or $L < 2.3$ fm are excluded from the final analysis resulting in the omission of the six leftmost data points and the blue data point around $m_\pi L \approx 4.5$. Note that the ratios are formed using the results for the second charm hopping parameter (κ_{c^2}), see table 3 in appendix A. For the $m_\pi \approx 286$ MeV ensembles, the lattice spacing is $a = 0.064$ fm, while for all others $a = 0.085$ fm.

5 Finite-volume effects

In this analysis, our goal is to ensure that all systematics are under control, including effects arising from simulating on a finite spatial volume. The latter are expected to be small for heavy meson observables, such as the mass [42] and decay constant. We test this expectation by analysing ensembles with the same light and strange quark masses and gauge coupling but different spatial extents. The volume dependence of m_D and f_D for five sets of ensembles is shown in figure 4. These ensembles cover a range in the pion mass from $m_\pi \approx 423$ MeV down to 220 MeV and in the spatial extent from 2.1 fm up to 4.1 fm, with $2.8 \le m_\pi L \le 5.9$. In particular, for $m_\pi \approx 286$ MeV, we have results for five different values of L. Modulo fluctuations in the data, the heavy-light meson mass tends to increase as $m_\pi L$ falls below 4, while no clear dependence can be resolved for the decay constant, although we cannot exclude a small decrease for $m_\pi L \lesssim 3$. To be conservative, we omit all ensembles with $m_\pi L < 3.5$ or $L < 2.3$ fm, namely ensembles S100, S201, U101, U102, U103, X252, X253. Among the remaining 40 ensembles, no dependence on the volume within uncertainties is found. This also holds for the heavy-strange meson masses and decay constants and light-light and light-strange meson masses, which also enter the analysis. Therefore, we decide not to perform an explicit infinite-volume extrapolation of the remaining data. For completeness, the volume dependence of m_{D_s}, f_{D_s}, m_π and m_K is given in figure 12 in appendix B.

6 Chiral and continuum extrapolation

To determine the decay constants at the physical point of isospin symmetric, $2 + 1$ flavour QCD, we extrapolate to the continuum limit and evaluate the decay constants for physical light, strange and charm quark mass. In our setup the approach to the continuum is controlled by ensembles with larger-than-physical light quark masses at six values of the lattice spacing, whereas the light and strange quark mass dependence is tightly constrained at

the physical point and the SU(3) symmetric point by ensembles which lie on three trajectories in the quark mass plane (see section 2 for more details). We perform a combined fit to the heavy-light and heavy-strange decay constants, which by construction are equal on the ensembles with SU(3) symmetry. Flavour symmetry provides further strong restrictions on the description of the data.

The charm quark is partially quenched in our setup. On each ensemble, the charmed observables are evaluated for two values of the heavy quark mass that encompass the physical charm quark mass. We choose not to interpolate our data to the physical point ensemble-by-ensemble but instead to fit all the data together and to account for the heavy quark mass dependence in the fit parametrisation. As there are 80 data points in total in the vicinity of the charm quark mass, this enables us to go beyond a simple linear interpolation.

6.1 Fixing the hadronic scheme

External input is required to set the lattice spacing in physical units, as well as to adjust the simulated masses of the light, strange and charm quarks to match those in nature. As described in succeeding subsections, this is realised by evaluating fits to the lattice spacing and meson mass dependence of the decay constants at the physical point, which therefore must be specified and defines our hadronic scheme. For scale setting, we employ the physical value of the gradient flow scale [43], $\sqrt{t_0^{\mathrm{phys}}} = 0.1449^{(7)}_{(9)}$ fm, determined utilising the Ξ baryon mass from ref. [3]. In the light quark sector, we define the physical point in isospin symmetric QCD using the values for the pion and kaon masses given in FLAG's 2016 review [44],

$$m_\pi = 134.8(3)\,\mathrm{MeV}\,, \qquad m_\mathrm{K} = 494.2(3)\,\mathrm{MeV}\,. \tag{6.1}$$

In the heavy quark sector, one would ideally fix the (valence) charm quark mass using a quantity that can be determined very accurately and that is largely insensitive to the dynamical light and strange (sea) quark content of the ensembles. One such quantity is the mass of the pseudoscalar charmonium meson. This choice introduces a small intrinsic imprecision, because in our analysis we neglect the quark-line disconnected contributions to the corresponding mass-degenerate pseudoscalar correlation function used to extract the charmonium mass, and likewise QED effects are omitted. To account for this, for the physical η_c meson mass we adopt the result $m_{\eta_\mathrm{c}} = 2978.3(1.1)\,\mathrm{MeV}$ quoted in ref. [45] and originally calculated in ref. [46]. It applies to pure $N_\mathrm{f} = 2 + 1 + 1$ QCD, i.e. in the absence of quark-disconnected diagrams and QED effects, and thus complies with our situation especially in these respects. Compared to the experimental value, $m_{\eta_\mathrm{c}}^{\mathrm{exp}} = 2983.9(4)\,\mathrm{MeV}$ [47], there is a $5.6\,\mathrm{MeV}$ shift such that we advocate as η_c input, fixing the charm quark mass, the central value from [45] with a $6\,\mathrm{MeV}$ error, viz.

$$m_{\eta_\mathrm{c}} = 2978(6)\,\mathrm{MeV}\,. \tag{6.2}$$

We are confident that $6\,\mathrm{MeV}$ reasonably quantifies the systematic uncertainty on our m_{η_c} input, which is dominantly due to ignoring the impact of charm annihilation to gluons. This is supported by ref. [46], where the latter was estimated to be $7.3(1.2)\,\mathrm{MeV}$, and is also in line with calculations that include the disconnected diagrams [48–50]. The value (6.2)

is also among the physical inputs entering the $N_\mathrm{f} = 2 + 1$ mixed-action study [11] with maximally twisted Wilson valence fermions.

Alternatively, one can tune the heavy-strange meson mass to the $\mathrm{D_s}$ mass. As explained in ref. [51], correcting the experimental result for the absence of electromagnetic effects that were estimated in ref. [52], $m_{\mathrm{D_s}}$ assumes the value

$$m_{\mathrm{D_s}} = 1966.0(4)\,\mathrm{MeV}\,. \tag{6.3}$$

This mass is approximately constant across the ensembles along the $\widehat{m}_\mathrm{s} \approx \mathrm{const.}$ trajectory, but varies along the $\mathrm{Tr}M = \mathrm{const.}$ and symmetric lines.

A third possibility is to match the flavour average of heavy-light and heavy-strange meson masses with the flavour averaged D meson mass. Taking $m_\mathrm{D} = 1866.1(2)$, again from ref. [51] in the isospin-symmetric limit of QCD and upon subtracting the electromagnetic mass contributions, then yields as physical input for the flavour average:

$$m_{\bar{\mathrm{D}}} = \frac{2}{3}m_\mathrm{D} + \frac{1}{3}m_{\mathrm{D_s}} = 1899.4(3)\,\mathrm{MeV}\,. \tag{6.4}$$

This combination is our preferred choice, as it remains almost constant along the $\mathrm{Tr}M = \mathrm{const.}$ trajectory, i.e. at constant physical flavour average of pion and kaon masses (denoted as $\bar{\mathbb{M}}^2_\mathrm{phys}$ in section 2), for which we have the most ensembles. Nevertheless, we also fix the physical charm quark mass using the η_c and $\mathrm{D_s}$ masses to check the sensitivity of our results to the matching procedure.

Lastly, for the sake of completeness, it should be mentioned that at a preliminary stage of our work [14, 15], we had also explored the spin-flavour averaged meson mass to fix the charm quark mass: its construction as a suitable linear combination of heavy-light and heavy-strange pseudoscalar and vector meson masses is guided by heavy-quark symmetry, and its use was also tested in ref. [53]. However, since the vector meson correlators are considerably noisier than the pseudoscalar ones (even if they allow extracting the ground state mass reliably), the statistical errors of the vector meson masses are still relatively large. Consequently, we do not observe any gain in overall statistical precision when including the spin-flavour averaged meson mass in the combined chiral-continuum fits and hence disregard it from our final analysis.

6.2 The loss function

To describe the dependence on the light, strange and heavy quark masses and on the lattice spacing, we use the independent variables t_0, m_π, m_K, $m_{\bar{\mathrm{D}}^1}$, $m_{\bar{\mathrm{D}}^2}$ in the fits (or $\{m_{\mathrm{D_s}^1}, m_{\mathrm{D_s}^2}\}$ or $\{m_{\eta_\mathrm{c}^1}, m_{\eta_\mathrm{c}^2}\}$ in the alternative schemes). The dependent variables for the simultaneous fit of heavy-light and heavy-strange decay constants for two values of the heavy quark mass per ensemble are $f_{\mathrm{D_s}^1}$, $f_{\mathrm{D_s}^2}$, f_{D^1} and f_{D^2}. We use the method described in appendix F.4 of ref. [3] to promote independent variables to fit parameters in order to take their uncertainty and correlation with the dependent variables into account. For a fully correlated fit we have to compute a 9×9 covariance matrix per ensemble, which reduces to 6×6 on ensembles with SU(3) symmetry. As different Monte Carlo chains are not correlated with each other, the full covariance matrix of the fit is block diagonal.

In practice, we fit the bare matrix elements of the $\mathrm{O}(a)$ improved axial vector current defined in eq. (4.3) with a fit function which describes the renormalised $\mathrm{O}(a)$ improved decay

constants (outlined in the next section) divided by the factor (cf. eqs. (3.3) and (3.4))

$$Z_{\mathrm{A}}\left(1 + b_{\mathrm{A}} a m_{q\mathrm{c}}\right) = Z_{\mathrm{A}}\left(1 + b_{\mathrm{A}}\left(\frac{1}{4\kappa_q} + \frac{1}{4\kappa_{\mathrm{c}}} - \frac{1}{2\kappa_{\mathrm{crit}}}\right)\right). \tag{6.5}$$

This approach enables us to take the uncertainties in the renormalisation and improvement factors and the critical hopping parameter (which all only depend on the gauge coupling) consistently into account. Treating these quantities as external input, we introduce Bayesian priors and widths (3 priors per β, with 18 priors in total) which are set to the central values and uncertainties, respectively, listed in table 6. Following ref. [3], the full loss function that is minimised in the fit corresponds to

$$\chi^2 = \sum_{e=1}^{n_e} \sum_{i,i'=1}^{N} \delta f_e^i (C_e^{-1})^{ii'} \delta f_e^{i'} + \sum_{j=1}^{18} \left(\frac{\delta p_j}{\Delta p_j}\right)^2 \tag{6.6}$$

where n_e is the number of ensembles, $N = 9$ or 6 is the number of observables for each ensemble, δf_e is the difference of the data and our model, C_e is the covariance matrix for ensemble e, δp_j is the difference of the prior and the corresponding fit parameter and Δp_j is the width of the prior. We remark that the prior fit parameters, obtained from the minimisation, agree within errors with the prior values. We make use of the Cholesky-decomposition of the covariance matrix

$$(C_e^{-1})^{ii'} = (L_e)^{ik}(L_e^T)^{ki'}, \tag{6.7}$$

to rewrite the $n_e \times N$ residuals as

$$r_e^k = \delta f_e^i (L_e)^{ik}, \tag{6.8}$$

which leads to the final form

$$\chi^2 = \sum_{e=1}^{n_e} \sum_{k=1}^{N} r_e^k (r_e^T)^k + \sum_{j=1}^{18} \left(\frac{\delta p_j}{\Delta p_j}\right)^2. \tag{6.9}$$

The loss function is minimised using the Levenberg-Marquardt algorithm in the `scipy` package [54, 55].

6.3 The fit model

Having defined the loss function, we now introduce the models used to describe our data. We simultaneously fit to the dimensionless combinations $\sqrt{8t_0}f_{\mathrm{D}}$ and $\sqrt{8t_0}f_{\mathrm{D_s}}$, where t_0 is the gradient flow scale. The light, strange and charm quark dependence of the decay constants is expressed in terms of the basis

$$\bar{M}^2 := \frac{1}{3}\left(2m_{\mathrm{K}}^2 + m_\pi^2\right) \propto (2m_{\mathrm{l}} + m_{\mathrm{s}}), \qquad \delta M^2 := 2\left(m_{\mathrm{K}}^2 - m_\pi^2\right) \propto (m_{\mathrm{s}} - m_{\mathrm{l}}), \tag{6.10}$$

$$\bar{M}_{\mathrm{H}} := m_{\bar{\mathrm{D}}} = \frac{2}{3}m_{\mathrm{D}} + \frac{1}{3}m_{\mathrm{D_s}} \propto m_{\mathrm{c}}, \tag{6.11}$$

and, similarly, we form dimensionless combinations to give,

$$\bar{\mathsf{M}}^2 := 8t_0 \bar{M}^2, \quad \delta\mathsf{M}^2 := 8t_0 \delta M^2, \quad \bar{\mathsf{M}}_{\mathrm{H}} := \sqrt{8t_0}\bar{M}_{\mathrm{H}}. \tag{6.12}$$

To begin with, we consider the light and strange quark mass dependence of the decay constants in the continuum limit at fixed charm quark mass. The leading terms in our ansätze are inspired by next-to-leading order (NLO) SU(3) heavy meson chiral perturbation theory (HMχPT) [56] and read

$$\sqrt{8t_0}f_{\mathrm{D_s}} = f_0 + c_1\,\bar{\mathsf{M}}^2 + \frac{2}{3}c_2\,\delta\mathsf{M}^2 + c_3\left(4\mu_{\mathrm{K}} + \frac{4}{3}\mu_\eta\right), \tag{6.13}$$

$$\sqrt{8t_0}f_{\mathrm{D}} = f_0 + c_1\,\bar{\mathsf{M}}^2 - \frac{1}{3}c_2\,\delta\mathsf{M}^2 + c_3\left(3\mu_\pi + 2\mu_{\mathrm{K}} + \frac{1}{3}\mu_\eta\right), \tag{6.14}$$

where the chiral logarithms are defined as

$$\mu_X = 8t_0 m_X^2 \log(8t_0 m_X^2) \tag{6.15}$$

with $X \in \{\pi, \mathrm{K}, \eta\}$, and the mass of the η meson is given by the Gell-Mann-Okubo relation

$$m_\eta^2 \approx \frac{4}{3}m_{\mathrm{K}}^2 - \frac{1}{3}m_\pi^2 = \bar{M}^2 + \frac{1}{3}\delta M^2. \tag{6.16}$$

Note that SU(3) symmetry constrains the coefficients of the expansion, with $f_{\mathrm{D}} = f_{\mathrm{D_s}}$ when $\delta\mathsf{M}^2 = 0$, and, to this order, only four low energy constants are needed to parameterise both decay constants. If we assume NNLO SU(3) ChPT [57] for the dependence of t_0 on the quark masses, the rescaling of $f_{\mathrm{D_{(s)}}}$ with $\sqrt{8t_0}$ does not introduce any additional terms in eqs. (6.13) and (6.14).

Turning to the heavy quark mass dependence, we only have to describe this dependence in a small region around the physical charm quark mass. We consider terms proportional to $\bar{\mathsf{M}}_{\mathrm{H}}$, $\delta\mathsf{M}^2\bar{\mathsf{M}}_{\mathrm{H}}$, $\bar{\mathsf{M}}^2\bar{\mathsf{M}}_{\mathrm{H}}$ and $\bar{\mathsf{M}}_{\mathrm{H}}^2$, among others (see below). Such terms arise when expanding in the difference between $\bar{\mathsf{M}}_{\mathrm{H}}$ and its value at the physical point.[3]

We use the gradient flow scale determined on each ensemble, t_0/a^2, to parameterise the lattice spacing dependence,

$$\mathfrak{a}^2 := \frac{a^2}{8t_0} = \frac{a_{\mathrm{chiral}}^2(g_0^2)}{8t_{0,\mathrm{chiral}}} + \mathrm{O}(a^2\bar{\mathsf{M}}^2), \tag{6.17}$$

where $t_{0,\mathrm{chiral}}$ is the value of t_0 in the chiral limit. The value of the lattice spacing in the chiral limit at g_0^2 is labelled as $a_{\mathrm{chiral}} \equiv \lim_{M\to 0} a(g_0^2, a\mathrm{Tr}M)$. Note that, assuming ChPT to hold, the leading order correction (starting at $a^2\bar{\mathsf{M}}^2$) originates from the correction to t_0 at NNLO SU(3) ChPT. As we are simulating at fixed g_0^2 (not fixed $\tilde{g}_0^2$), discretisation effects enter as (small) order $a^3\bar{\mathsf{M}}^2$ corrections, and order $a^4\bar{\mathsf{M}}^2$ and $a^4\delta\mathsf{M}^2$ effects arise due to $\mathrm{O}(a^2)$ corrections on t_0/a^2. Each of the above terms is taken into account in our fit models as part of the description of the discretisation effects.

Our ansatz for the lattice spacing effects is guided by Symanzik effective theory [58, 59]. After full $\mathrm{O}(a)$ improvement of the action and observables, cutoff effects start at order a^2. Due to the relatively large mass of the charm quark, we expect to resolve mass-dependent

---

[3]An alternative approach, that is consistent with the heavy quark limit, would be to form the combinations $\sqrt{m_{\mathrm{D_{(s)}}}}f_{\mathrm{D_{(s)}}}$ and to expand in powers of $1/m_{\mathrm{D_{(s)}}}$. Given that the (global) interpolation to the physical charm quark mass is tightly constrained by the large number data points (see section 6.5), we expect this approach to yield very consistent results.

cutoff effects. As outlined in refs. [60, 61], quantum corrections to Symanzik effective theory may introduce discretisation effects of order $a^2[\bar{g}^2(1/a)]^{\hat{\gamma}_i}$, where $\bar{g}^2(1/a)$ is the renormalised coupling, leading to a logarithmic modification of the cutoff effects. In refs. [61, 62] it has been found that the smallest anomalous dimension $\hat{\gamma}_i$ for pseudoscalar and axial vector currents is 0 for our action and there is no dangerous slowing down of the continuum extrapolation. We assume that contributions from terms with $\hat{\gamma}_i > 0$ are subleading and consider terms proportional to $\mathfrak{a}^2$, $\mathfrak{a}^2\bar{\mathbb{M}}^2$, $\mathfrak{a}^2\delta\mathbb{M}^2$, $\mathfrak{a}^2\bar{\mathbb{M}}_{\mathrm{H}}$ and higher powers in $\mathfrak{a}$, as detailed below.

We construct global fit models by combining the individual terms for the dependence on the light, strange and heavy quark masses and on the inverse cutoff additively, such that the models are linear in the fit parameters. By investigating the fit quality, we compose a model with a minimal number of parameters that is able to describe our data reasonably well,

$$\sqrt{8t_0}f_{\mathrm{D_s}}(m_\pi, m_{\mathrm{K}}, m_{\bar{\mathrm{D}}}, a) = f_0 + c_1\bar{\mathbb{M}}^2 + \frac{2}{3}c_2\,\delta\mathbb{M}^2 + c_3\left(4\mu_{\mathrm{K}} + \frac{4}{3}\mu_\eta\right) \qquad + c_4\bar{\mathbb{M}}_{\mathrm{H}} \quad (6.18)$$
$$+ c_5\bar{\mathbb{M}}_{\mathrm{H}}^2 + c_6\,\delta\mathbb{M}^2\bar{\mathbb{M}}_{\mathrm{H}} + c_8\bar{\mathbb{M}}^2\bar{\mathbb{M}}_{\mathrm{H}} + c_9\mathfrak{a}^2 + c_{10}\mathfrak{a}^2\bar{\mathbb{M}}_{\mathrm{H}}\,,$$

$$\sqrt{8t_0}f_{\mathrm{D}}(m_\pi, m_{\mathrm{K}}, m_{\bar{\mathrm{D}}}, a) = f_0 + c_1\bar{\mathbb{M}}^2 - \frac{1}{3}c_2\,\delta\mathbb{M}^2 + c_3\left(3\mu_\pi + 2\mu_{\mathrm{K}} + \frac{1}{3}\mu_\eta\right) + c_4\bar{\mathbb{M}}_{\mathrm{H}}$$
$$+ c_5\bar{\mathbb{M}}_{\mathrm{H}}^2 + c_7\,\delta\mathbb{M}^2\bar{\mathbb{M}}_{\mathrm{H}} + c_8\bar{\mathbb{M}}^2\bar{\mathbb{M}}_{\mathrm{H}} + c_9\mathfrak{a}^2 + c_{10}\mathfrak{a}^2\bar{\mathbb{M}}_{\mathrm{H}}\,.$$

Only eleven parameters are needed to describe the 160 naive degrees of freedom, which are effectively reduced due to the correlation in the data. The fit quality for this fully correlated fit is $\chi^2/\mathrm{d.o.f} = 1.08$. Omitting terms in eq. (6.18), e.g. setting any of $c_{5-8,10}$ to zero, leads to a significant increase in the χ^2. Note that the above expressions are consistent with SU(3) constraints and there is only one fit parameter (c_6 respectively c_7) that is not shared by the ansätze for f_{D} and $f_{\mathrm{D_s}}$. We find that, in addition to the linear term, we have to incorporate a term that is quadratic in $\bar{\mathbb{M}}_{\mathrm{H}}$ which could not have been resolved when fixing the charm quark mass ensemble by ensemble prior to the extrapolation. Furthermore, mixed terms involving the heavy quark mass and the sea quark mass proxies are necessary to achieve a good description of the data. In terms of lattice spacing effects, mass-independent contributions and those dependent on the heavy quark are dominant.

To explore the parameter space of the extrapolation and to test for higher order effects, we build a variety of models, which extend eq. (6.18). We add up to four terms out of the following list of higher order terms in the quark masses,

$$\bar{\mathbb{M}}^2\bar{\mathbb{M}}_{\mathrm{H}}^2\,, \quad \bar{\mathbb{M}}^2\delta\mathbb{M}^2\,, \quad (\delta\mathbb{M}^2)^2\,, \quad \delta\mathbb{M}^2\bar{\mathbb{M}}_{\mathrm{H}}^2\,, \quad (\delta\mathbb{M}^2)^2\bar{\mathbb{M}}_{\mathrm{H}}\,, \quad (6.19)$$

and up to three terms out of the following lists of terms describing lattice artifacts,

$$\mathfrak{a}^2\bar{\mathbb{M}}^2\,, \quad \mathfrak{a}^2\delta\mathbb{M}^2\,, \quad \mathfrak{a}^3\,, \quad \mathfrak{a}^3\bar{\mathbb{M}}^2\,, \quad \mathfrak{a}^3\delta\mathbb{M}^2\,, \quad \mathfrak{a}^3\bar{\mathbb{M}}_{\mathrm{H}}\,, \quad \mathfrak{a}^4\,, \quad \mathfrak{a}^4\bar{\mathbb{M}}^2\,, \quad \mathfrak{a}^4\delta\mathbb{M}^2\,, \quad \mathfrak{a}^4\bar{\mathbb{M}}_{\mathrm{H}}\,. \quad (6.20)$$

We exclude models that mix a^3 and a^4 cutoff effects and models with more than 16 parameters. In total this amounts to $K = 482$ models. The worst fit quality found in this set has a fully correlated $\chi^2/\mathrm{d.o.f.} = 1.09$. The best fit quality of the models under consideration is

found to be $\chi^2/\text{d.o.f.} = 0.92$ for the model,

$$
\sqrt{8t_0} f_{D_s}(m_\pi, m_K, m_{\bar{D}}, a) = f_0 + c_1 \bar{\mathbb{M}}^2 + \frac{2}{3} c_2 \,\delta\mathbb{M}^2 + c_3 \left(4\mu_K + \frac{4}{3}\mu_\eta\right) \qquad + c_4 \bar{\mathbb{M}}_H \quad (6.21)
$$
$$
+ c_5 \bar{\mathbb{M}}_H^2 + c_6 \,\delta\mathbb{M}^2 \bar{\mathbb{M}}_H + c_8 \bar{\mathbb{M}}^2 \bar{\mathbb{M}}_H + c_9 \,\mathfrak{a}^2 + c_{10}\, \mathfrak{a}^2 \bar{\mathbb{M}}_H
$$
$$
+ c_{11} \,\delta\mathbb{M}^2 \bar{\mathbb{M}}_H^2 + c_{13} \,\mathfrak{a}^3 + c_{14} \,\mathfrak{a}^3 \delta\mathbb{M}^2\,,
$$
$$
\sqrt{8t_0} f_D(m_\pi, m_K, m_{\bar{D}}, a) = f_0 + c_1 \bar{\mathbb{M}}^2 - \frac{1}{3} c_2 \,\delta\mathbb{M}^2 + c_3 \left(3\mu_\pi + 2\mu_K + \frac{1}{3}\mu_\eta\right) + c_4 \bar{\mathbb{M}}_H
$$
$$
+ c_5 \bar{\mathbb{M}}_H^2 + c_7 \,\delta\mathbb{M}^2 \bar{\mathbb{M}}_H + c_8 \bar{\mathbb{M}}^2 \bar{\mathbb{M}}_H + c_9 \,\mathfrak{a}^2 + c_{10}\, \mathfrak{a}^2 \bar{\mathbb{M}}_H
$$
$$
+ c_{12} \,\delta\mathbb{M}^2 \bar{\mathbb{M}}_H^2 + c_{13} \,\mathfrak{a}^3 + c_{14} \,\mathfrak{a}^3 \delta\mathbb{M}^2\,.
$$

Especially the inclusion of higher order cutoff effects, such as the terms multiplying c_{13} and c_{14} in eq. (6.21), is found to improve the fit quality with respect to the base fit.

6.4   Model averages

For our final result, we take into account all the information that we derive from the set of K fits defined above, by performing a weighted average over the results. The weight that is assigned to a model k is based on the Akaike information criterion (AIC) [63, 64],

$$
\text{AIC}_k = \chi_k^2 + 2M_k\,, \tag{6.22}
$$

where M_k is the number of model parameters and the loss function χ^2 is defined in eq. (6.9). The AIC introduces a penalty for each additional fit parameter, such that fits with less parameters are preferred over fits with more parameters but similar χ^2. The weight for each model reads

$$
w_k^{\text{AIC}} = N \exp\left(-\frac{1}{2}\text{AIC}_k\right)\,, \tag{6.23}
$$

where the normalisation N is chosen such that $\sum_{k=1}^{K} w_k^{\text{AIC}} = 1$. The central value for an observable $\mathcal{O}$ is computed from a weighted average over all models,

$$
\mathcal{O} = \sum_{k=1}^{K} w_k^{\text{AIC}} \mathcal{O}_k\,, \tag{6.24}
$$

where $\mathcal{O}_k$ is the result for the observable based on model k. The statistical error is also obtained from this weighted average via standard error propagation for derived observables. Following ref. [65], we estimate the systematic uncertainty, stemming from the variation in the model space, from the width of the distribution of the results in the model average,

$$
\sigma_{\text{sys}}^2 = \sum_{k=1}^{K} w_k^{\text{AIC}} \mathcal{O}_k^2 - \left(\sum_{k=1}^{K} w_k^{\text{AIC}} \mathcal{O}_k\right)^2\,. \tag{6.25}
$$

The fit with the largest model weight of 0.025 is also the fit with the smallest $\chi^2/\text{d.o.f.}$, i.e. the one of eq. (6.21). The fit with the smallest contribution to the average has a weight of $2 \cdot 10^{-6}$. The model average does not include cuts on the data, e.g. excluding the data points for the largest value of $\bar{\mathbb{M}}^2$ or $\mathfrak{a}$. This is because the base model in eq. (6.18), without
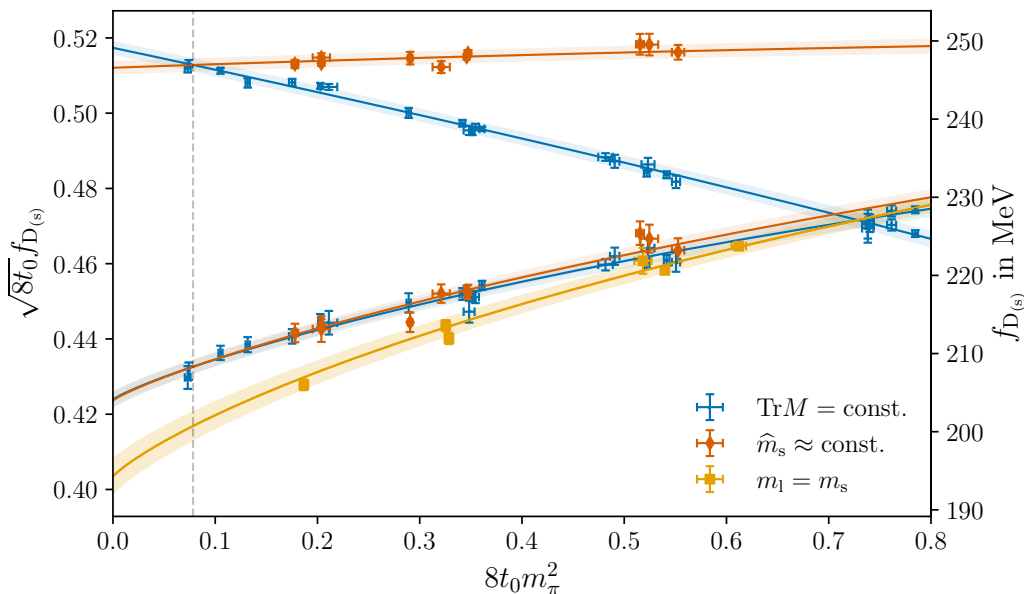
Figure 5. Dependence of f_D and f_{D_s} on the pion mass squared for the fit with the largest AIC weight (eq. (6.21)), with all quantities in dimensionless combinations with the gradient flow scale t_0. The data points are corrected for effects due to the cutoff and mistuning of the light and strange quark mass and shifted to the physical charm quark mass, see the text. The results lie on three trajectories, for which $\mathrm{Tr}M = \text{const.}$, $\widehat{m}_s \approx \text{const.}$ and $m_l = m_s$, as described in section 2 and displayed in figure 1. The central value and error band of the fit in the continuum limit, for the physical charm quark mass, is projected onto these trajectories. The vertical dashed line indicates the physical point.

higher order terms in lattice spacing or quark masses, adequately represents the entire dataset. However, we explicitly test that fitting the base model remains consistent when applying cuts in the lattice spacing, the pion mass, the sea quark parameter $\bar{\mathbb{M}}^2$ or the heavy quark parameter $\bar{\mathbb{M}}_H$. Among this set of cuts, the most pronounced impact stems from cuts in the lattice spacing. The exclusion of ensembles at the coarsest lattice spacings leads to a small downward shift of the decay constants (and a slight upward shift of their ratio). A similar effect is observed when including terms that allow for $O(a^3)$ or $O(a^4)$ cutoff effects when fitting the full data set, as it is the case in eq. (6.21).

6.5 Illustration of the quark mass and cutoff dependence

We use the fit with the largest model weight (eq. (6.21)) to illustrate the dependence of f_D and f_{D_s} on the quark masses and the cutoff. In figure 5, we display the light quark mass dependence, where the fit is used to correct the results for lattice spacing effects, mistuning of the light and strange quark masses (see the discussion in section 2) and to shift to the physical charm quark mass. In terms of the mistuning, for a given pion mass, the strange quark mass is fixed implicitly by the chiral trajectories: the data on the $\mathrm{Tr}M = \text{const.}$ and $\widehat{m}_s \approx \text{const.}$ trajectories are shifted to correspond to the kaon mass which gives the physical value of $\bar{M}^2 = (2m_K^2 + m_\pi^2)/3 \propto 2m_l + m_s$ and $2m_K^2 - m_\pi^2 \propto m_s$, respectively. At the physical point, the continuum fit curves projected onto these two trajectories (coloured blue and orange, respectively) have to coincide by definition, tightly constraining the fit. The fit curves
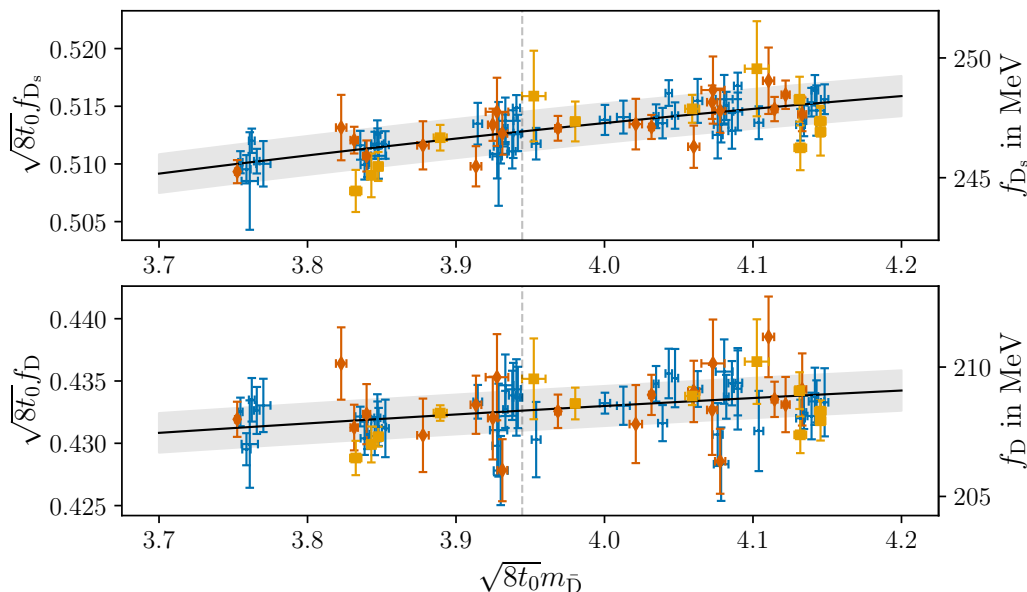
Figure 6. Dependence of f_D and f_{D_s} on the flavour average D meson mass for the fit with the largest AIC weight, as shown in figure 5. The dashed line indicates the physical value of $\sqrt{8t_0}m_{\bar{D}}$. The data points are shifted using the fit to the physical pion and kaon masses and lattice spacing effects are removed. The central value and error for the corresponding $m_{\bar{D}}$ dependence of the fit are shown as the black line and grey band, respectively.

clearly show that the strange quark effects on f_D are small, while f_{D_s} is largely insensitive to the light quark mass, when keeping the strange quark mass at its physical value.

Along the symmetric line (yellow curve), which approaches the SU(3) chiral limit when lowering the pion mass, the f_D and f_{D_s} decay constants are equal. Including the data on this trajectory helps to constrain the dependence on the parameter $\bar{\mathbb{M}}^2$. Flavour breaking effects are observed for the results on the $\text{Tr}M = \text{const.}$ trajectory, starting from the SU(3) symmetric point and decreasing the pion mass towards the physical point. The curvature due to the chiral logarithms can be mapped out thanks to the two ensembles at physical pion mass and several further ensembles with $m_\pi < 200\,\text{MeV}$.

The heavy quark mass dependence of the decay constants, parameterised by $\bar{\mathbb{M}}_H$ in eq. (6.21), is presented in figure 6. Note that the data points are corrected for all cutoff effects (including those arising from the $\mathfrak{o}^2\bar{\mathbb{M}}_H$ terms) and shifted to correspond to the physical light and strange quark masses. Two charm quark masses are realised per ensemble and, overall, the results bracket the physical value of the flavour average D meson mass, indicated by the dashed line. By performing a global fit of the heavy quark mass dependence, we are able to resolve terms quadratic in $\bar{\mathbb{M}}_H$. However, as seen in the figure, these contributions are rather minor.

Figure 7 shows the projection of the best fit onto the cutoff dependence for physical quark masses. Discretisation effects are a significant source of systematics for observables involving charm quarks, with $am_c \approx 0.5$ for our coarsest lattice spacing. However, by utilising high statistics data at six lattice spacings ranging from $a \approx 0.10\,\text{fm}$ down to $a = 0.039\,\text{fm}$ (a^2 varies
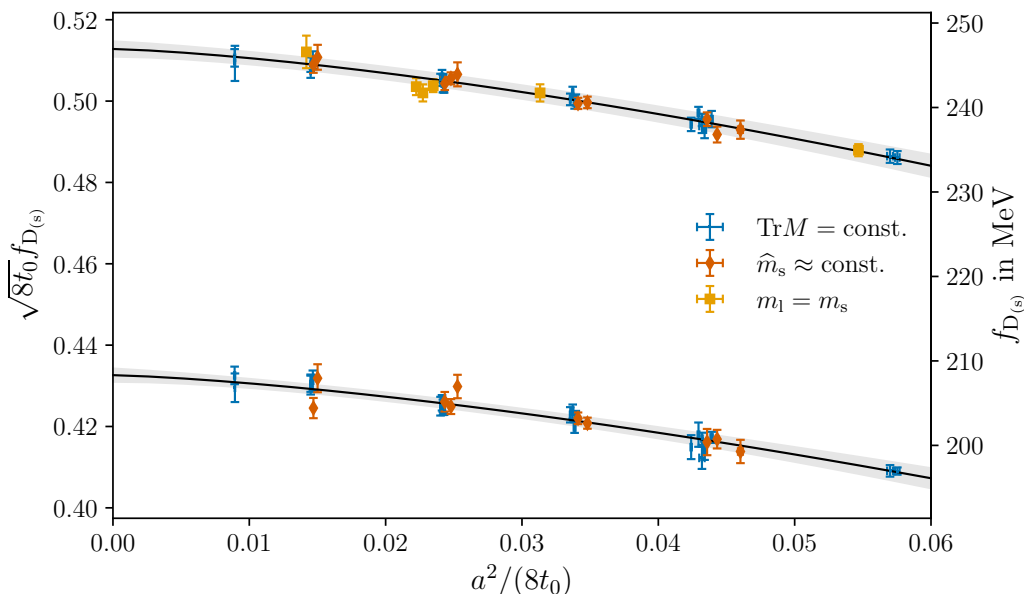
Figure 7. Dependence of f_D and f_{D_s} on the lattice spacing squared for the fit with the largest AIC weight, as shown in figure 5. The data points are shifted using the fit to the physical pion, kaon and $\bar{D}$ meson masses. The central value and error for the corresponding lattice spacing dependence of the fit are shown as the black line and grey band, respectively.

by more than a factor of 6), we are able to clearly resolve the lattice spacing dependence, including both $\mathfrak{a}^2$ and $\mathfrak{a}^3$ terms. With full non-perturbative $O(a)$ improvement, the size of these effects is fairly moderate with a 5% difference between the decay constants at the coarsest lattice spacing and in the continuum limit. When varying the fit model, we found that fits including $\mathfrak{a}^3$ or $\mathfrak{a}^4$ terms were favoured by the data. This is illustrated in figure 8 which shows the lattice spacing dependence for all fits considered. The variation of the ansatz to describe the cutoff effects, as illustrated in the figure, is the main contribution to our final systematic uncertainty.

7 Results

Employing the isospin-corrected experimental pion, kaon and flavour average D meson masses given in section 6.1 and the physical value of the flow scale of ref. [3], we extract results for the decay constants at the physical point (in the continuum limit) in physical units for each of the 482 fits considered. For the ratio f_{D_s}/f_D, we simply divide the results at the physical point for the individual decay constants. Alternatively, one can perform a simultaneous continuum, chiral extrapolation of the ratio directly. While only a reduced number of terms would need to be included in the model for such a fit (many terms cancel when taking the ratio of the two fit forms, for instance, in eq. (6.21)), the data set entering the fit would be much reduced. In particular, results from ensembles with SU(3) symmetry would not be included. As our simultaneous fits to f_D and f_{D_s} take all correlations into account, we would not expected to obtain more precise results by fitting to the ratio. Following the model averaging procedure
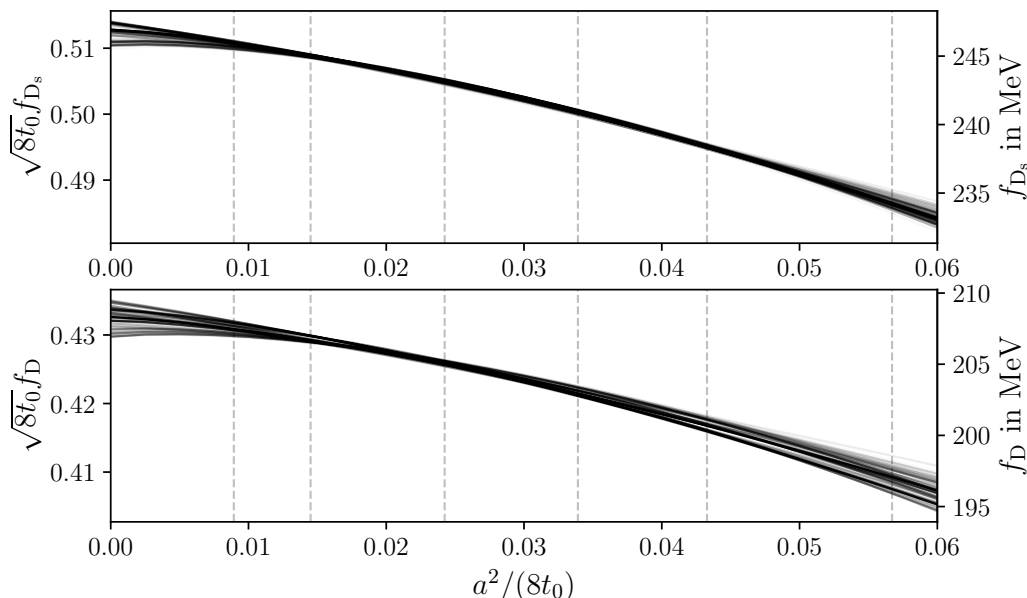
Figure 8. Illustration of the lattice spacing dependence of all fits considered. Each line corresponds to the central value of one model that enters the model average. The opacity of a line indicates the relative model weight, with a black line corresponding to the highest weight. The dashed lines show the six values of the lattice spacing where the fit is constrained by data.

outlined in section 6.4, our final results at the physical point of $N_\text{f} = 2 + 1$ flavour QCD read

$$
\begin{aligned}
f_{\text{D}_\text{s}} &= 246.8(0.64)_\text{stat}(0.61)_\text{sys}(0.95)_\text{scale}[1.3]\,\text{MeV}\,, \\
f_\text{D} &= 208.4(0.67)_\text{stat}(0.75)_\text{sys}(1.11)_\text{scale}[1.5]\,\text{MeV}\,, \\
f_{\text{D}_\text{s}}/f_\text{D} &= 1.1842(21)_\text{stat}(22)_\text{sys}(19)_\text{scale}[36]\,,
\end{aligned}
\tag{7.1}
$$

where the first error is statistical, the second is due to the systematics and the third arises from the scale setting. The statistical error includes the uncertainties due to the renormalisation and improvement coefficients and the hadronic scheme, while the systematic error quantifies the uncertainty stemming from the model variation for continuum and quark mass extrapolations or interpolations. The total uncertainty obtained by adding the individual errors in quadrature is given within the square brackets. We achieve a 0.5%, 0.7% and 0.3% overall error in f_{D_s}, f_D and $f_{\text{D}_\text{s}}/f_\text{D}$, respectively. The results for the ratio indicate that SU(3) flavour symmetry breaking effects in the decay constants are around 20% at the physical point.

We illustrate the variation in the results across the 482 fits in figure 9. This shows the distributions of the central values, where each fit contributes to the histograms according to its AIC weight. For both the individual decay constants and the ratio, the spread in the values is mainly due to the variation in the parametrisation of the discretisation effects, i.e. the uncertainty arising from the continuum limit extrapolation dominates the systematic error (indicated by the grey band). In particular, a slight double peak structure visible in the histogram for the ratio is due to the inclusion or exclusion of $\text{O}(a^3)$ or $\text{O}(a^4)$ cutoff effects in the model. However, this variation is well within the full uncertainty of the final result (shown as dashed lines).
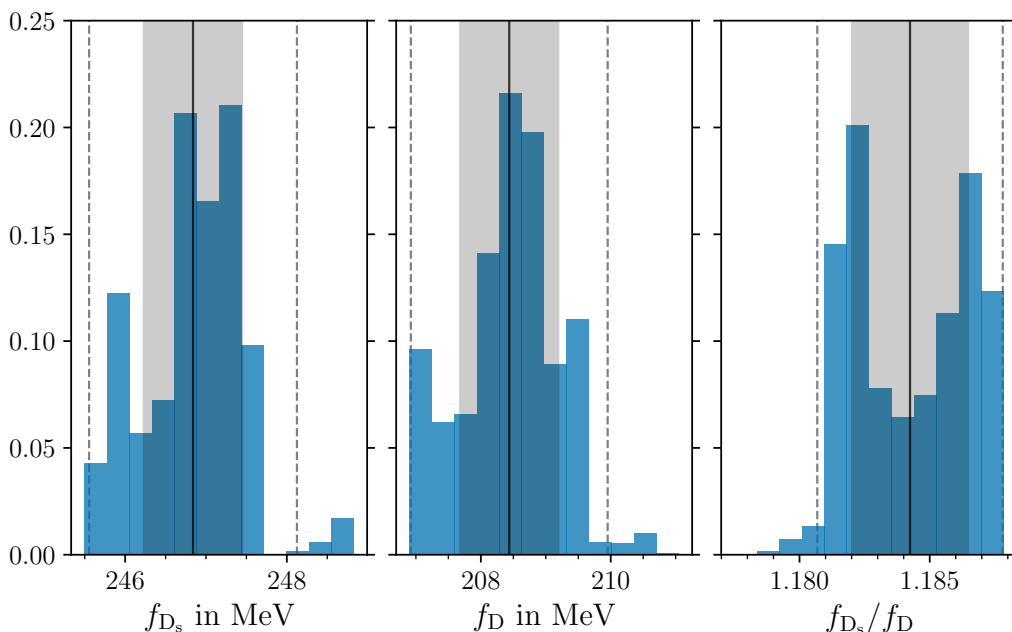
Figure 9. AIC weighted histograms of the central values of f_{D_s}, f_D and their ratio obtained from the 482 fits that enter our model averaging procedure. The solid lines indicates the central values of the final results, the grey bands display the corresponding systematic errors and the dotted lines show the total uncertainties.

	f_{D_s}	f_D	f_{D_s}/f_D
Scale setting	53.5%	55.1%	27.8%
Systematic error	22.3%	24.8%	39.0%
Statistical error			
Gauge ensembles	20.5%	18.3%	32.0%
Renormalisation and improvement	3.6%	1.8%	0.8%
Physical meson masses	0.1%	0.0%	0.4%

Table 1. Relative contributions to the squared total errors of the final results.

The full error budget can be found in table 1. The uncertainty due to the scale setting dominates the total in the case of f_D and f_{D_s} and contributes to the error of the ratio via the definition of the physical point. The systematic uncertainties are of a similar size as the statistical uncertainties from the fluctuations of the gauge configurations. The renormalisation and improvement coefficients [8, 10] are determined precisely enough that they only account for a few percent of the total squared error. Similarly, the errors due to the physical inputs that define the physical point are negligible. While the systematic uncertainties are computed according to eq. (6.25), we track the contribution of all other sources of error to the variance as part of the error propagation in the Γ method.

In our $N_{\rm f} = 2 + 1$ simulation, where the charm quark is partially quenched, we neglect strong isospin breaking and QED effects, as well as the effect of charm quark loops in the sea. For low-energy observables, the latter are expected to be negligible due to the decoupling of the heavy quark [66]. However, for heavy-light quantities, for which there is no clear separation of scales, the omission of charm loops may lead to a small but significant effect. Parametrically, this effect is of $O(\alpha_{\rm s}(\Lambda_{\rm QCD}/2m_{\rm c})^2)$ [67, 68] for the decay constants, which amounts to about 0.5%.[4] In the ratio of the two decay constants, this effect is further suppressed by $(m_{\rm s} - m_{\rm d})/\Lambda_{\rm QCD} \sim 0.4$, resulting in an overall effect of about 0.2%. In ref. [72], the effect of charm quark loops on charmonium decay constants has been investigated non-perturbatively. Comparing the pseudoscalar decay constants obtained from a pure Yang-Mills background with their counterparts from a sea with two charm quarks, the authors found an increase at the level of 0.5%. With respect to our work, this represents a very conservative upper bound since it quantifies the effect from two heavy sea quarks for an observable with two heavy valence quarks.

Turning to the effects of strong isospin breaking, with light quarks in the valence sector, the leading effects for $f_{\rm D}$ are linear in the up and down quark mass difference and are of $O((m_{\rm u} - m_{\rm d})/\Lambda_{\rm QCD}) \sim 0.6\%$. So far, these effects have only have been estimated on the lattice by FNAL/MILC in their $N_{\rm f} = 2+1+1$ study [12] by tuning to the physical up and down quark masses. They find $f_{\rm D+} - f_{\rm D} = 0.58(7)\,{\rm MeV}$ and $f_{\rm D+} - f_{\rm D^0} = 1.11(15)\,{\rm MeV}$. This is consistent with QCD sum rule estimates from Lucha et al., who find $f_{\rm D+} - f_{\rm D^0} = 0.97(13)\,{\rm MeV}$ [73]. For $f_{\rm D_s}$, strong isospin breaking effects only arise due to the light sea quarks. They are quadratic in the mass difference and are likely to be much smaller in magnitude than for $f_{\rm D}$.

Electromagnetic interactions are expected to enter at the level of $O(\alpha_{\rm QED}) \sim 1\%$. As it is difficult to separate leptonic decays including a photon in the final state from those only with a lepton and a neutrino in experiment, both virtual and real radiative corrections to the decay rate need to be considered. In this case, the decay rate can no longer be factorised into a decay constant and a term involving the relevant CKM matrix element. The experimental decay rates are adjusted using estimates of these radiative effects (see, for example, the PDG review of leptonic decays of charged pseudoscalar mesons [47]) in order to extract the combinations $f_{\rm D}|V_{\rm cd}|$ and $f_{\rm D_s}|V_{\rm cs}|$ in a particular scheme. Lattice calculations of the leading QED corrections, including the determination of the form factors for radiative leptonic decays, such as $D_{\rm s} \to \ell\nu\gamma$ [74, 75], are ongoing.

We conclude that the effect of the missing charm quark loops and isospin breaking in our calculation is likely to be around the same size as or below our total uncertainties. However, the absence of these effects also impacts on the predictions for the decay constants indirectly through the determination of the lattice scale and the tuning of the quark masses. As the precision increases, the results will depend on the hadronic scheme, with a number of different schemes being employed in the literature. In order to facilitate a close comparison with other lattice studies (which use t_0 to set the scale), we give the dependence of the decay constants and their ratio on the input parameters that define our scheme at linear order in

---

[4]For this and the following estimates quoted in the text, we use result for $\Lambda_{\rm QCD}$ from ref. [69], the charm quark mass as calculated in ref. [53], the values of the light and strange quark masses quoted in ref. [70] and the determination of $m_u - m_d$ presented in ref. [71].

appendix C. This allows the results to be shifted to take into account small modifications of the scheme. In the appendix, we also collect the values of the decay constants for the two schemes where the charm quark mass is fixed from the mass of the D_s and the η_c meson. The choice of scheme has very little impact on the results.

From our results for f_D and f_{D_s}, we can compute the CKM matrix elements $|V_{cd}|$ and $|V_{cs}|$. The PDG [47] lists the products of decay constants and CKM matrix elements, derived from the experimental $D^+ \to \ell\nu[\gamma]$ and $D_s^+ \to \ell\nu[\gamma]$ decay rates, as

$$f_{D^+}|V_{cd}| = 45.82(1.10)\,\text{MeV}\,, \qquad f_{D_s^+}|V_{cd}| = 243.5(2.7)\,\text{MeV}\,, \qquad (7.2)$$

respectively, where the uncertainty is due to the estimation of the radiative corrections and the measured branching fractions. Together with our results in eq. (7.1), we obtain

$$|V_{cd}| = 0.2199(15)(52)[55]\,, \qquad |V_{cs}| = 0.987(5)(10)[13]\,, \qquad (7.3)$$

where the first error is due to our lattice results and the second arises from the combined experimental and non-lattice theory uncertainty in eq. (7.2). Note that we have not included the systematic uncertainties due to the omission of strong isospin breaking and charm loop effects (estimated previously). These uncertainties are small compared to the total error, which is dominated by the combined non-lattice uncertainty. The above values are consistent with, but slightly less precise than, those quoted by the PDG (that are derived from the same leptonic decay rates [47]). The PDG utilise the FLAG report $N_f = 2+1+1$ results [13] for the decay constants, which have smaller errors than ours, as discussed below. The CKM matrix elements can also be determined from the decay rates for the semi-leptonic decays $D \to \pi\ell\nu$ and $D_s \to K\ell\nu$ and lattice calculations of the corresponding form factors. At present, the PDG value for $|V_{cd}|$ obtained from the leptonic decay is more precise, while for $|V_{cs}|$ the value extracted from the semi-leptonic decay rate has smaller uncertainties.

There is a long history of calculating f_D and f_{D_s} on the lattice. In figure 10, we compare our values with recent $N_f = 2+1$ and $N_f = 2+1+1$ determinations. Only those results that consider all sources of systematic uncertainty in their analysis and pass the quality criteria of the FLAG 21 review [13] (for the continuum limit, chiral and finite volume extrapolations, renormalisation and the treatment of the heavy quark) are shown. We also only display the latest results for each collaboration. Further recent works can be found in refs. [83–85]. Note that the ALPHA 23 study of ref. [11] utilises a small subset of the ensembles employed in the present analysis and we expect some statistical correlation with our values. They include ten ensembles with $m_\pi \geq 200\,\text{MeV}$ on the $\text{Tr}M = \text{const.}$ trajectory in a mixed action setup with maximally twisted Wilson valence fermions.

For the $N_f = 2+1$ theory, our results are the most precise and represent a significant improvement on earlier studies. All works are in reasonable agreement with each other. FNAL/MILC [12] quote the smallest total uncertainties of around $0.3(0.2)\%$ for $f_D(f_{D_s})$ and 0.1% for f_{D_s}/f_D, and their results dominate the FLAG average for $N_f = 2+1+1$. At this level of precision, the definition of isospin symmetric QCD has a significant impact on the values of the decay constants. Note that we compare to the isospin symmetric result for f_D given in ref. [12] and follow the FLAG report [13] by rescaling the central value given for $f_{D_s}/f_{D^+} = 1.1749(16)$ by the ratio of the central values for f_{D^+} and f_D to obtain
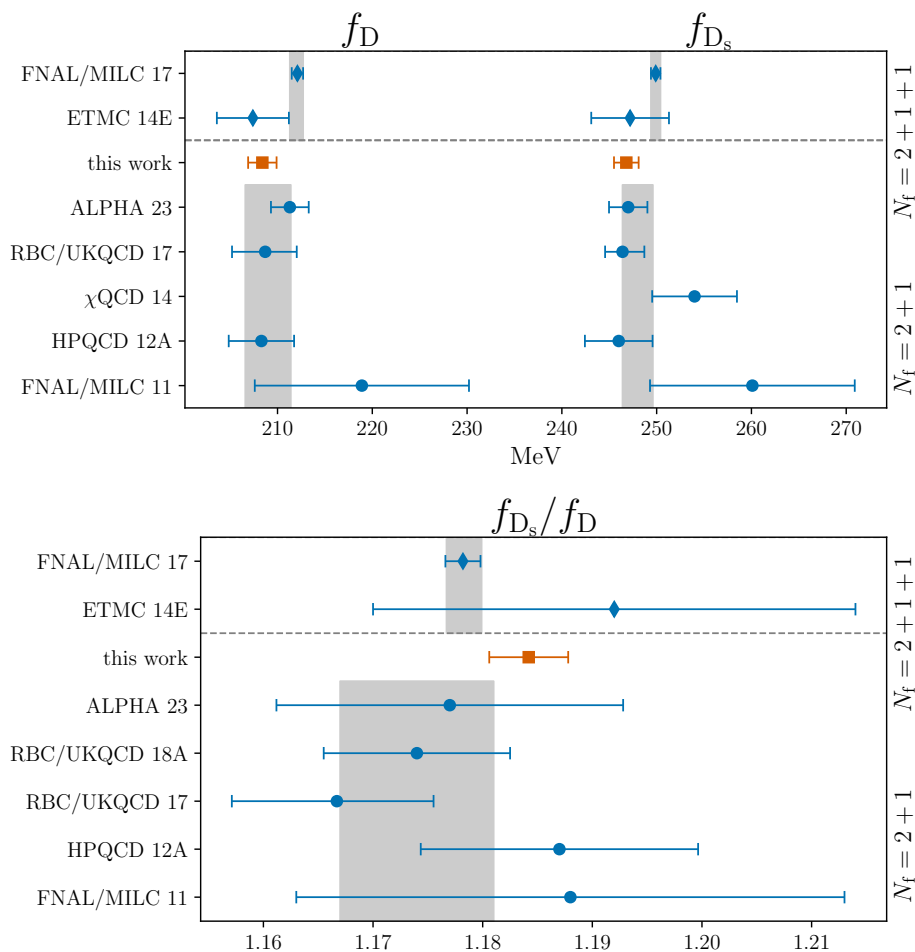
Figure 10. Comparison of lattice results for the decay constants f_D and f_{D_s} (top) and their ratio (bottom) for $N_f = 2 + 1$ [11, 76–81] and $N_f = 2 + 1 + 1$ [12, 82]. Only results that fulfil all the FLAG quality criteria and that are not superseded by later works are displayed. The grey bands show the FLAG 21 averages from ref. [13].

$f_{D_s}/f_D = 1.1782(16)$. The FNAL/MILC results for the individual decay constants lie roughly 2σ above ours, while the results for the ratio are slightly more consistent. These differences are not statistically significant and, as argued above, the absence of charm quark loop effects in our simulations is likely to lead to a less than one sigma effect.

8 Conclusions

In this work, we determine the leptonic decay constants of the D and D_s mesons in $2 + 1$ flavour lattice QCD with Wilson fermions. We utilise 49 high statistics ensembles at six values of the lattice spacing, which lie on three distinct quark mass trajectories covering a wide range of light and strange quark masses. This enables us to achieve an excellent description of both the cutoff effects and the quark mass dependence down to the physical point. The charm-light and charm-strange decay constants are fitted simultaneously, with all correlations taken into account, and a large set of parameterisations is considered in order to reliably

quantify the systematics associated with the continuum limit and chiral extrapolation. Our final results are summarised in eq. (7.1) and a full error budget is given in table 1. A 0.5%, 0.7% and 0.3% overall uncertainty is achieved for f_{D_s}, f_D and f_{D_s}/f_D, respectively. These are the most precise $2+1$ flavour results to-date. When simulating isospin symmetric QCD, it is important to specify the hadronic scheme used to set the scale and tune the quark masses. In appendix C we give the dependence of the results on the hadronic input, allowing for a close comparison with other works, where t_0 is used to set the lattice scale.

Further improvement in the determination of the decay constants would require a more precise evaluation of the scale, followed by a reduction in both the statistical and systematic errors. The main source of the latter error is the continuum extrapolation. The discretisation effects are moderate but significant, with a 5% difference in the values of the decay constants at the coarsest lattice spacing and those in the continuum limit. Furthermore, we resolve cutoff effects beyond the leading order of $O(a^2)$. Additional ensembles at the finest lattice spacing of $a = 0.039\,\mathrm{fm}$ with quark masses closer to their physical values would help to further constrain the extrapolation. Generating even finer lattices than the ones employed in this work is challenging, even with state-of-the-art algorithms, due to the critical slowing down that is observed towards the continuum limit [18].

The charm quark is partially quenched in our analysis. The effect of charm quark loops on the decay constants may not depend strongly on the light and strange quark masses, and an estimate of the size of this effect could be made at the SU(3) symmetric point (corresponding to $m_\pi = m_K \approx 410\,\mathrm{MeV}$), using the ensembles of this work and the $3+1$ flavour ensembles of ref. [86]. However, the renormalisation factor for the axial vector current for the $3+1$ flavour theory, along with the associated $O(a)$ improvement coefficients, would need to be computed for such comparison to be meaningful.

Acknowledgments

A Tables

Table 2. Overview of analysed ensembles along the three quark mass plane trajectories where the light equals the strange quark mass (sym), the average bare quark mass is constant (TrM), and the strange quark mass is approximately constant (m_s); ensemble name (id), (p)eriodic or (o)pen boundary conditions (bc) in time, pion and the kaon masses in physical units (see also table 4 for raw masses including errors) as well as the spatial (L) and temporal (T) lattice extent in physical units and the spatial extent in units of the pion mass. The lattice spacing a is taken from ref. [3]. Optimized number n_i of smearing iterations for light ($i = $ l), strange ($i = $ s), and charm ($i = $ c $\equiv$ c$^1 = $ c^2) quark. Number of sources N_src used to calculate point-to-all propagators on a configuration and total number of configurations N_conf analysed. Analysed configurations are separated by Δ molecular dynamic units. Note that for ensembles with open boundary conditions a certain number of time slices have not been considered in the computation of some observables for sources close to the boundary due to boundary effects, see discussion in the text. Ensembles marked with a star do not enter the final extrapolation.

traj.	id	bc	$\frac{m_\pi}{\text{MeV}}$	$\frac{m_\text{K}}{\text{MeV}}$	$\frac{L}{\text{fm}}$	$\frac{T}{\text{fm}}$	$m_\pi L$	n_l	n_s	n_c	N_src	N_conf	Δ
					$\beta = 3.34, a = 0.098\,\text{fm}$								
sym	A650	p	370	370	2.34	4.69	4.39	160	160	19	12	5062	4
TrM	A653	p	430	430	2.34	4.69	5.10	150	150	19	12	2525	8
	A654	p	335	458	2.34	4.69	3.98	185	165	19	12	2533	8
					$\beta = 3.4, a = 0.085\,\text{fm}$								
	U103*	o	420	420	2.05	10.9	4.35	220	220	25	9	2475	8
	H101	o	423	423	2.73	8.19	5.85	220	220	25	20	2016	4
	U102*	o	358	445	2.05	10.9	3.71	250	210	25	37	1561	8
	H102	o	358	444	2.73	8.19	4.95	250	210	25	20	1920	4
TrM	U101*	o	273	465	2.05	10.9	2.83	300	200	25	37	1964	4
	H105	o	284	467	2.73	8.19	3.93	300	200	25	20	1827	4

Table 2. Overview of analysed ensembles (continued).

traj.	id	bc	$\frac{m_\pi}{\text{MeV}}$	$\frac{m_K}{\text{MeV}}$	$\frac{L}{\text{fm}}$	$\frac{T}{\text{fm}}$	$m_\pi L$	n_l	n_s	n_c	N_{src}	N_{conf}	Δ
	N101	o	281	467	4.09	10.9	5.83	300	200	25	37	1593	4
	S100*	o	211	475	2.73	10.9	2.92	350	170	25	37	983	4
	C101	o	220	473	4.09	8.19	4.57	350	170	25	20	2530	4
	D150	p	129	482	5.46	10.9	3.56	440	140	25	32	602	4
	H107	o	369	550	2.73	8.19	5.10	250	160	25	18	1064	4
m_s	H106	o	276	519	2.73	8.19	3.82	250	160	25	18	1506	4
	C102	o	218	503	4.09	8.19	4.52	350	160	25	18	1496	4
$\beta = 3.46, a = 0.075\,\text{fm}$													
sym	X450	p	264	264	3.62	4.83	4.85	400	400	30	32	1059	4
	B450	p	421	421	2.42	4.83	5.15	270	270	30	16	1612	4
	S400	o	354	445	2.42	9.66	4.33	310	260	30	21	2872	4
TrM	N451	p	289	466	3.62	9.66	5.31	375	250	30	32	1011	4
	D450	p	216	480	4.83	9.66	5.29	480	200	30	32	544	4
	D452	p	155	487	4.83	9.66	3.80	530	180	30	32	995	4
	B452*	p	352	548	2.42	4.83	4.31	310	200	30	16	1944	4
m_s	N450	p	287	527	3.62	9.66	5.27	375	200	30	32	1130	4
	D451	p	218	507	4.83	9.66	5.34	480	200	30	32	1028	4
$\beta = 3.55, a = 0.064\,\text{fm}$													
	X250	p	348	348	3.06	4.08	5.41	445	445	45	32	1500	4
sym	X251	p	267	267	3.06	4.08	4.15	540	540	45	32	1411	4
	D250	p	199	199	4.08	8.17	4.12	660	660	45	32	458	4
	N202	o	414	414	3.06	8.17	6.42	390	390	45	20	899	4
	N203	o	348	445	3.06	8.17	5.40	445	375	45	21	1543	4
	S201*	o	294	471	2.04	8.17	3.04	540	360	45	20	1955	8
	X252*	p	288	467	2.30	8.17	3.35	540	360	45	32	3508	4
TrM	X253*	p	287	466	2.55	8.17	3.71	540	360	45	32	3005	4
	N200	o	286	466	3.06	8.17	4.45	540	360	45	21	1712	4
	D251	p	286	465	4.08	8.17	5.91	540	360	45	32	403	4
	D200	o	201	481	4.08	8.17	4.16	660	290	45	20	1999	4
	E250	p	130	493	6.13	12.3	4.05	795	285	45	32	503	4
	N204	o	353	548	3.06	8.17	5.48	445	285	45	24	1500	4
m_s	N201	o	287	527	3.06	8.17	4.45	540	285	45	24	1522	4

Continued on next page

Table 2. Overview of analysed ensembles (continued).

traj.	id	bc	$\frac{m_\pi}{\text{MeV}}$	$\frac{m_\text{K}}{\text{MeV}}$	$\frac{L}{\text{fm}}$	$\frac{T}{\text{fm}}$	$m_\pi L$	n_l	n_s	n_c	N_src	N_conf	Δ
	D201	o	204	506	4.08	8.17	4.21	660	285	45	20	1078	4
$\beta = 3.7, a = 0.049\,\text{fm}$													
sym	N306	o	343	343	2.37	6.32	4.12	750	750	75	21	1507	4
TrM	N300*	o	426	426	2.37	6.32	5.11	640	640	75	18	1540	4
	N302	o	350	454	2.37	6.32	4.20	750	620	75	21	2201	4
	J303	o	259	478	3.16	9.48	4.14	950	525	75	20	999	8
	E300	o	175	495	4.74	9.48	4.20	800	310	55	16	1137	4
m_s	N304	o	355	556	2.37	6.32	4.26	750	465	75	24	1651	4
	J304	o	261	527	3.16	9.48	4.18	950	465	75	3	1521	4
$\beta = 3.85, a = 0.039\,\text{fm}$													
TrM	J500	o	414	414	2.48	7.44	5.20	1000	1000	115	3	1837	8
	J501	o	337	448	2.48	7.44	4.23	1225	1025	115	20	2292	4

Table 3. Hopping parameters used in the computation of the correlation functions. κ_l and κ_s match those that have been used in the generation of the ensemble. Ensembles marked with a star do not enter the final extrapolation.

traj.	id	κ_l	κ_s	κ_{c^1}	κ_{c^2}
$\beta = 3.34, a = 0.098\,\text{fm}$					
sym	A650	0.1366	0.1366	0.121904	0.120692
TrM	A653	0.1365715	0.1365715	0.121904	0.120692
	A654	0.13675	0.136216193	0.121904	0.120692
$\beta = 3.4, a = 0.085\,\text{fm}$					
TrM	U103*	0.13675962	0.13675962	0.124056	0.123147
	H101	0.13675962	0.13675962	0.124056	0.123147
	U102*	0.136865	0.136549339	0.124056	0.123147
	H102	0.136865	0.136549339	0.124056	0.123147
	U101*	0.13697	0.13634079	0.124056	0.123147
	H105	0.13697	0.13634079	0.124056	0.123147
	N101	0.13697	0.13634079	0.124056	0.123147
	S100*	0.13703	0.136222041	0.124056	0.123147
	C101	0.13703	0.136222041	0.124056	0.123147
	D150	0.137088	0.13610755	0.124056	0.123147

Continued on next page

Table 3. Overview of hopping parameters (continued).

traj.	id	κ_{l}	κ_{s}	κ_{c^1}	κ_{c^2}
	H107	0.13694566590798	0.136203165143476	0.124056	0.123147
m_{s}	H106	0.137015570024	0.136148704478	0.124056	0.123147
	C102	0.13705084580022	0.13612906255557	0.124056	0.123147
$\beta = 3.46, a = 0.075\,\mathrm{fm}$					
sym	X450	0.136994	0.136994	0.1254266	0.12617097
	B450	0.13689	0.13689	0.1258025	0.12503
	S400	0.136984	0.136702387	0.126983423	0.125563292
TrM	N451	0.1370616	0.1365480771	0.126983423	0.125563292
	D450	0.137126	0.136420428639937	0.126983423	0.125563292
	D452	0.137163675	0.136345904546	0.126983423	0.125563292
	B452*	0.1370455	0.136378044	0.1258025	0.12503
m_{s}	N450	0.1370986	0.136352601	0.1258025	0.12503
	D451	0.13714	0.136337761	0.126983423	0.125563292
$\beta = 3.55, a = 0.064\,\mathrm{fm}$					
	X250	0.13705	0.13705	0.12751596	0.12871743
sym	X251	0.1371	0.1371	0.12765893	0.12884069
	D250	0.13713129	0.13713129	0.12884069	0.12765893
	N202	0.137	0.137	0.128651119	0.1274374
	N203	0.13708	0.136840284	0.128651119	0.1274374
	S201*	0.13714	0.13672086	0.128651119	0.1274374
	X252*	0.13714	0.13672086	0.128651119	0.1274374
TrM	X253*	0.13714	0.13672086	0.128651119	0.1274374
	N200	0.13714	0.13672086	0.128651119	0.1274374
	D251	0.13714	0.13672086	0.128651119	0.1274374
	D200	0.1372	0.136601748	0.128651119	0.1274374
	E250	0.137232867	0.136536633	0.128651119	0.1274374
	N204	0.137112	0.136575049	0.128651119	0.1274374
m_{s}	N201	0.13715968	0.136561319	0.128651119	0.1274374
	D201	0.1372067	0.136546844	0.128651119	0.1274374
$\beta = 3.7, a = 0.049\,\mathrm{fm}$					
sym	N306	0.13705013	0.13705013	0.13062697	0.13018588

Continued on next page

Table 3. Overview of hopping parameters (continued).

traj.	id	κ_l	κ_s	κ_{c^1}	κ_{c^2}
TrM	N300*	0.137	0.137	0.13062697	0.13018588
	N302	0.137064	0.1368721791358	0.13062697	0.13018588
	J303	0.137123	0.1367546608	0.13062697	0.13018588
	E300	0.137163	0.136675163617733	0.13062697	0.13018588
m_s	N304	0.137079325093654	0.136665430105663	0.13062697	0.13018588
	J304	0.13713	0.1366569203	0.13062697	0.13018588
$\beta = 3.85, a = 0.039\,\mathrm{fm}$					
TrM	J500	0.136852	0.136852	0.13242984	0.13206693
	J501	0.1369032	0.136749715	0.13242984	0.13206693

Table 4. The gluonic observable t_0/a^2 and the pseudoscalar masses that are used in the extrapolation to the physical point in lattice units. Ensembles marked with a star do not enter the final extrapolation.

traj.	id	t_0/a^2	am_π	am_K	$am_{\bar{D}^1}$	$am_{\bar{D}^2}$
$\beta = 3.34, a = 0.098\,\mathrm{fm}$						
sym	A650	2.2860(76)	0.1829(13)	0.1829(13)	0.90948(53)	0.94916(52)
TrM	A653	2.1727(62)	0.2125(10)	0.2125(10)	0.91999(51)	0.95951(50)
	A654	2.1932(83)	0.1657(14)	0.2268(11)	0.91846(53)	0.95798(55)
$\beta = 3.4, a = 0.085\,\mathrm{fm}$						
TrM	U103*	2.8841(63)	0.18138(75)	0.18138(75)	0.82103(62)	0.85207(65)
	H101	2.8468(56)	0.18285(67)	0.18285(67)	0.82029(49)	0.85132(51)
	U102*	2.888(12)	0.1546(11)	0.19240(78)	0.81953(60)	0.85049(63)
	H102	2.8806(75)	0.15458(66)	0.19208(74)	0.81819(60)	0.84913(63)
	U101*	2.926(13)	0.1178(25)	0.2011(13)	0.81845(73)	0.84946(78)
	H105	2.894(13)	0.1227(10)	0.20196(76)	0.81686(75)	0.84771(78)
	N101	2.8930(32)	0.12153(53)	0.20172(31)	0.81758(27)	0.84850(29)
	S100*	2.9223(89)	0.0914(40)	0.20528(75)	0.81651(71)	0.84742(77)
	C101	2.9105(47)	0.0952(19)	0.2043(14)	0.81666(51)	0.84754(54)
	D150	2.9475(34)	0.0557(11)	0.20840(29)	0.81425(54)	0.84513(57)
m_s	H107	2.716(11)	0.1595(11)	0.23777(89)	0.83190(71)	0.86265(76)
	H106	2.8208(58)	0.1193(16)	0.22428(78)	0.82381(66)	0.85469(68)
	C102	2.8684(53)	0.0942(20)	0.2173(13)	0.81931(66)	0.85015(70)

Continued on next page

Table 4. Overview of t_0/a^2 and pseudoscalar masses (continued).

traj.	id	t_0/a^2	am_π	am_K	$am_{\bar{D}^1}$	$am_{\bar{D}^2}$
			$\beta = 3.46, a = 0.075\,\mathrm{fm}$			
sym	X450	3.9901(85)	0.10098(43)	0.10098(43)	0.73124(40)	0.70450(33)
	B450	3.663(13)	0.16105(51)	0.16105(51)	0.73582(45)	0.76313(44)
	S400	3.6917(77)	0.13540(42)	0.17020(40)	0.69167(36)	0.74324(37)
TrM	N451	3.6821(66)	0.11069(42)	0.17826(25)	0.69183(24)	0.74340(26)
	D450	3.7068(57)	0.08270(48)	0.18355(19)	0.69092(32)	0.74249(36)
	D452	3.7266(36)	0.05939(61)	0.18638(15)	0.68970(31)	0.74128(35)
	B452*	3.5284(69)	0.13468(48)	0.20969(35)	0.74516(32)	0.77239(33)
m_s	N450	3.5919(47)	0.10972(35)	0.20177(23)	0.74035(25)	0.76756(28)
	D451	3.6645(52)	0.08337(27)	0.19381(16)	0.69308(25)	0.74461(27)
			$\beta = 3.55, a = 0.064\,\mathrm{fm}$			
	X250	5.321(16)	0.11261(28)	0.11261(28)	0.63537(30)	0.58974(31)
sym	X251	5.499(10)	0.08642(34)	0.08642(34)	0.62294(43)	0.57781(43)
	D250	5.619(14)	0.06444(53)	0.06444(53)	0.57317(40)	0.61829(45)
	N202	5.166(21)	0.13382(48)	0.13382(48)	0.59858(64)	0.64445(63)
	N203	5.1466(73)	0.11259(32)	0.14397(30)	0.59821(31)	0.64396(32)
	S201*	5.164(11)	0.09515(57)	0.15232(51)	0.59885(71)	0.64458(77)
	X252*	5.160(10)	0.09317(27)	0.15106(21)	0.59868(25)	0.64448(27)
TrM	X253*	5.1535(69)	0.09276(21)	0.15075(19)	0.59861(20)	0.64449(22)
	N200	5.1633(70)	0.09264(46)	0.15069(38)	0.59830(33)	0.64407(36)
	D251	5.1527(83)	0.09235(27)	0.15053(27)	0.59815(22)	0.64393(24)
	D200	5.1790(62)	0.06503(57)	0.15558(56)	0.59766(28)	0.64344(31)
	E250	5.2027(44)	0.04218(25)	0.159369(67)	0.59714(35)	0.64299(38)
	N204	4.947(10)	0.11413(47)	0.17729(42)	0.60767(43)	0.65342(46)
m_s	N201	5.0426(78)	0.09277(44)	0.17042(30)	0.60324(30)	0.64898(33)
	D201	5.1363(84)	0.06582(58)	0.16364(37)	0.59901(37)	0.64478(39)

Table 4. Overview of t_0/a^2 and pseudoscalar masses (continued).

traj.	id	t_0/a^2	am_π	am_K	$am_{\bar{D}^1}$	$am_{\bar{D}^2}$
			$\beta = 3.7, a = 0.049\,\mathrm{fm}$			
sym	N306	8.811(48)	0.08575(72)	0.08575(72)	0.47077(60)	0.48866(61)
TrM	N300*	8.566(39)	0.10649(45)	0.10649(45)	0.47366(65)	0.49153(68)
	N302	8.526(25)	0.08758(52)	0.11370(49)	0.47624(45)	0.49409(46)
	J303	8.620(15)	0.06476(26)	0.11963(20)	0.47466(28)	0.49250(29)
	E300	8.6193(63)	0.04371(35)	0.12395(32)	0.47422(24)	0.49204(25)
m_s	N304	8.328(25)	0.08873(76)	0.13923(68)	0.48117(62)	0.49899(63)
	J304	8.501(15)	0.06537(27)	0.13175(28)	0.47669(34)	0.49447(36)
			$\beta = 3.85, a = 0.039\,\mathrm{fm}$			
TrM	J500	13.973(28)	0.08127(30)	0.08127(30)	0.35574(43)	0.37159(46)
	J501	14.007(70)	0.06617(35)	0.08801(33)	0.35616(31)	0.37206(32)

Table 5. Bare decay constants in lattice units based on O(a) improved currents defined in eq. (3.2). Ensembles marked with a star do not enter the final extrapolation.

traj.	id	af_{D^1}	af_{D^2}	$af_{D_s^1}$	$af_{D_s^2}$
			$\beta = 3.34, a = 0.098\,\mathrm{fm}$		
sym	A650	0.10683(24)	0.10540(24)	0.10683(24)	0.10540(24)
TrM	A653	0.11141(25)	0.10990(26)	0.11141(25)	0.10990(26)
	A654	0.10797(38)	0.10644(40)	0.11477(25)	0.11326(27)
			$\beta = 3.4, a = 0.085\,\mathrm{fm}$		
TrM	U103*	0.10203(47)	0.10121(55)	0.10203(47)	0.10121(55)
	H101	0.10186(33)	0.10086(35)	0.10186(33)	0.10086(35)
	U102*	0.09913(47)	0.09814(49)	0.10362(31)	0.10261(33)
	H102	0.09863(55)	0.09761(58)	0.10331(36)	0.10229(38)
	U101*	0.09599(69)	0.09507(72)	0.10540(34)	0.10440(35)
	H105	0.09581(64)	0.09470(67)	0.10570(28)	0.10468(29)
	N101	0.09683(33)	0.09582(39)	0.10603(18)	0.10502(18)
	S100*	0.09424(75)	0.09325(78)	0.10707(23)	0.10606(24)
	C101	0.09501(67)	0.09393(71)	0.10716(16)	0.10613(16)
	D150	0.09148(64)	0.09042(67)	0.10732(22)	0.10628(23)
m_s	H107	0.10203(75)	0.10099(78)	0.11166(44)	0.11064(45)
	H106	0.09802(54)	0.09701(56)	0.10933(37)	0.10828(39)

Continued on next page

Table 5. Overview of bare decay constants (continued).

traj.	id	af_{D^1}	af_{D^2}	$af_{\mathrm{D}_{\mathrm{s}}^1}$	$af_{\mathrm{D}_{\mathrm{s}}^2}$
	C102	0.09531(74)	0.09422(79)	0.10916(25)	0.10814(26)
$\beta = 3.46, a = 0.075\,\mathrm{fm}$					
sym	X450	0.08331(31)	0.08402(28)	0.08331(31)	0.08402(28)
	B450	0.09228(26)	0.09157(25)	0.09228(26)	0.09157(25)
	S400	0.09138(29)	0.09007(31)	0.09594(19)	0.09465(20)
TrM	N451	0.09029(24)	0.08898(29)	0.098113(93)	0.09682(11)
	D450	0.08827(38)	0.08692(43)	0.09971(13)	0.09844(14)
	D452	0.08643(38)	0.08518(46)	0.10001(13)	0.09872(14)
	B452*	0.09352(31)	0.09281(33)	0.10232(14)	0.10156(14)
m_{s}	N450	0.08994(28)	0.08918(29)	0.10115(13)	0.10037(12)
	D451	0.08855(29)	0.08717(32)	0.10098(11)	0.09969(11)
$\beta = 3.55, a = 0.064\,\mathrm{fm}$					
	X250	0.07693(18)	0.07785(17)	0.07693(18)	0.07785(17)
sym	X251	0.07285(28)	0.07380(27)	0.07285(28)	0.07380(27)
	D250	0.07101(24)	0.07006(26)	0.07101(24)	0.07006(26)
	N202	0.08114(31)	0.08024(33)	0.08114(31)	0.08024(33)
	N203	0.07947(25)	0.07846(27)	0.08356(16)	0.08259(18)
	S201*	0.07655(86)	0.07551(91)	0.08515(33)	0.08419(38)
	X252*	0.07775(23)	0.07679(25)	0.08523(12)	0.08430(13)
TrM	X253*	0.07806(19)	0.07718(23)	0.08526(11)	0.08437(10)
	N200	0.07788(29)	0.07686(34)	0.08542(15)	0.08449(16)
	D251	0.07795(22)	0.07694(24)	0.08521(17)	0.08427(18)
	D200	0.07604(33)	0.07501(40)	0.08690(15)	0.08599(17)
	E250	0.07434(40)	0.07338(46)	0.08756(14)	0.08668(16)
	N204	0.08241(55)	0.08148(60)	0.09019(46)	0.08937(46)
m_{s}	N201	0.07901(34)	0.07802(40)	0.08910(15)	0.08824(16)
	D201	0.07651(43)	0.07553(51)	0.08799(18)	0.08706(20)

Table 5. Overview of bare decay constants (continued).

traj.	id	af_{D^1}	af_{D^2}	$af_{\mathrm{D}_{\mathrm{s}}^1}$	$af_{\mathrm{D}_{\mathrm{s}}^2}$
		$\beta = 3.7, a = 0.049\,\mathrm{fm}$			
sym	N306	0.06244(47)	0.06226(49)	0.06244(47)	0.06226(49)
	N300*	0.06374(43)	0.06345(45)	0.06374(43)	0.06345(45)
$\mathrm{Tr}M$	N302	0.06398(37)	0.06377(39)	0.06735(25)	0.06714(26)
	J303	0.06169(35)	0.06148(37)	0.06862(18)	0.06842(19)
	E300	0.06019(27)	0.05994(24)	0.06956(17)	0.06934(17)
m_{s}	N304	0.06505(53)	0.06485(54)	0.07194(40)	0.07176(39)
	J304	0.06138(36)	0.06111(37)	0.07078(23)	0.07061(24)
		$\beta = 3.85, a = 0.039\,\mathrm{fm}$			
$\mathrm{Tr}M$	J500	0.05136(42)	0.05128(44)	0.05136(42)	0.05128(44)
	J501	0.05045(26)	0.05036(25)	0.05320(20)	0.05315(21)

β	3.34	3.4	3.46	3.55	3.7	3.85
Z_{A} [8]	0.7510(11)	0.75629(65)	0.76172(39)	0.76994(34)	0.78356(32)	0.79675(45)
b_{A} [10]	1.249(16)	1.244(16)	1.239(15)	1.232(15)	1.221(13)	1.211(12)
c_{A} [9]	-0.055709847	-0.048973873	-0.04320929	-0.036074160	-0.027286251	-0.021260222
κ_{crit} [3]	0.1366938(45)	0.1369153(9)	0.1370613(10)	0.1371715(10)	0.1371530(9)	0.1369767(26)

Table 6. Summary table of input parameters used for the calculation of the decay constants. Note that c_{A} defines the valence action, so no uncertainty enters for this quantity. For κ_{crit} we use the values in ref. [3] labeled κ_{crit} (int), and b_{A} from eq. (5.4) in ref. [10] is used. Note that we set $\bar{b}_{\mathrm{A}}$ to zero because all coefficients in eq. (5.3) in ref. [10] are compatible with zero.
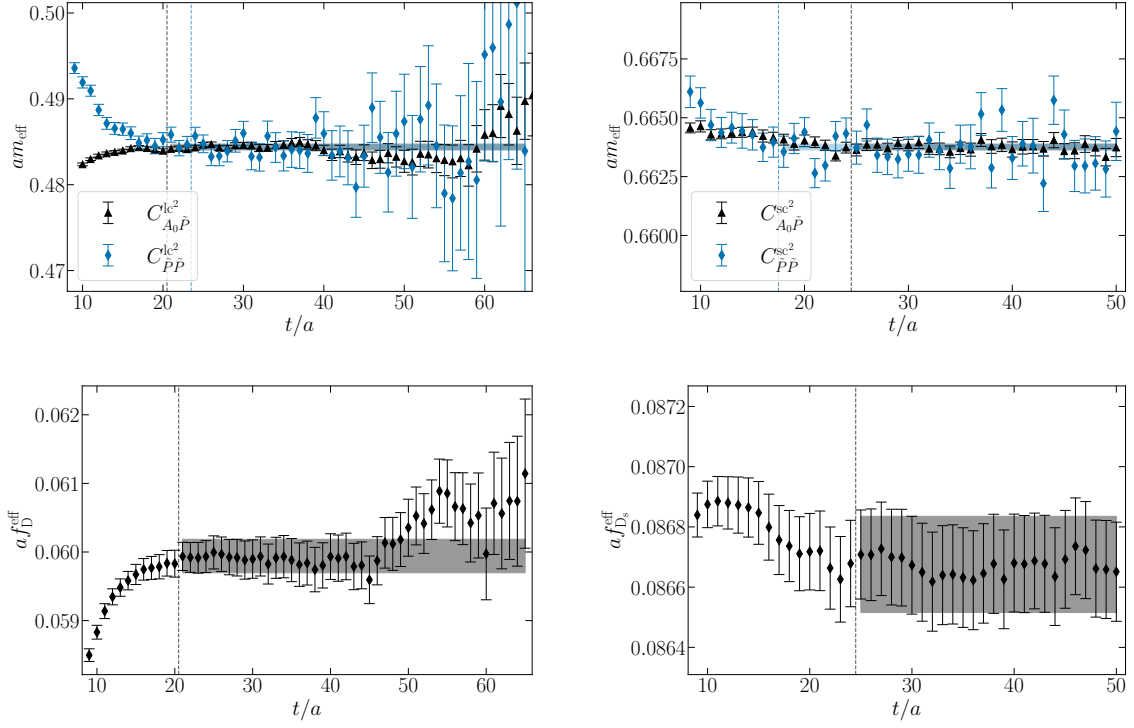
Figure 11. Results from our combined fits to the heavy-light current on E300 (left, $m_\pi = 175\,\text{MeV}$, $a = 0.049\,\text{fm}$) and the heavy-strange current on E250 (right, $m_\pi = 130\,\text{MeV}$, $a = 0.064\,\text{fm}$) as in figure 3.
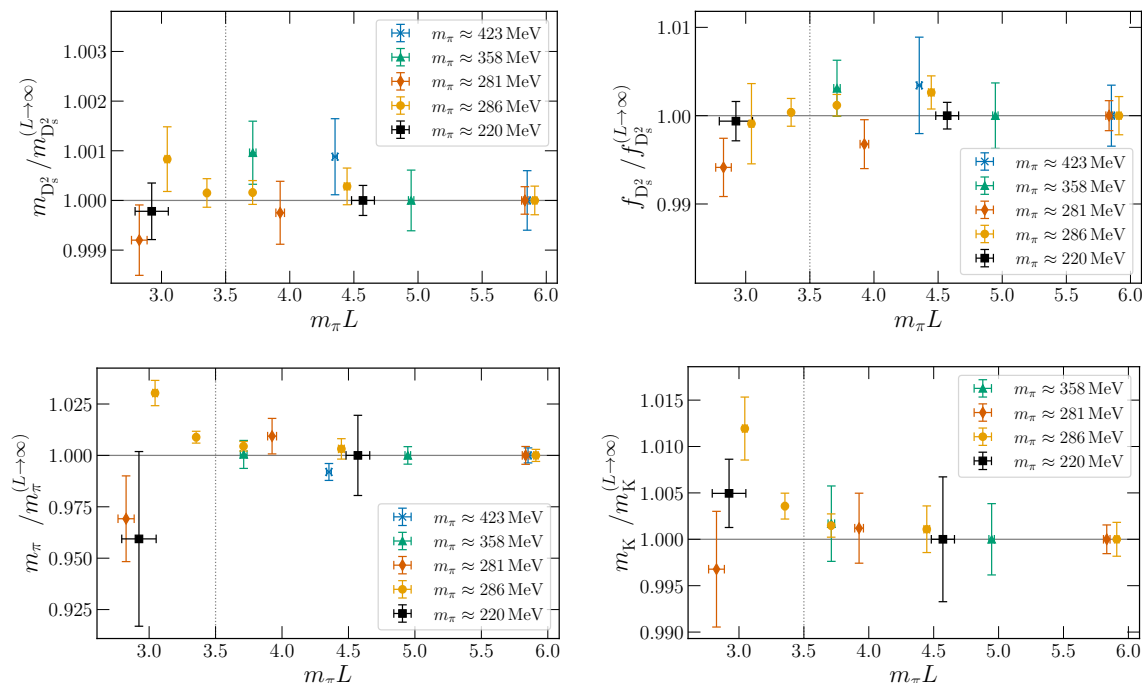
Figure 12. Volume dependence of the heavy-strange meson mass (top left) and decay constant (top right) and the pion mass (bottom left) and kaon mass (bottom right). The results are displayed as in figure 4.

C Scheme dependence

As outlined in the main text, in particular in section 6.1, an ambiguity with respect to the way isospin symmetric QCD is defined may be present when comparing results of different collaborations. To allow for a comparison of our result with other works without this ambiguity, we here collect our results based on three different schemes that differ in the matching of the charm quark mass.

In eq. (7.1) we have reported the results using the flavour averaged D meson mass to fix the mass of the charm quark. Using m_{D_s} we obtain

$$f_{D_s} = 247.0(1.4)\,\text{MeV}\,, \quad f_D = 208.7(1.6)\,\text{MeV}\,, \quad f_{D_s}/f_D = 1.1833(37)\,, \tag{C.1}$$

and with m_{η_c} we arrive at

$$f_{D_s} = 246.9(1.3)\,\text{MeV}\,, \quad f_D = 208.6(1.5)\,\text{MeV}\,, \quad f_{D_s}/f_D = 1.1838(34)\,. \tag{C.2}$$

The impact of switching between the three schemes is thus insignificant.

In table 7 we list the dependence of our final results in the three different schemes on the input quantities in the form $S\frac{\partial O}{\partial S}$ for the dependence of observable O on S. The derivatives allow to a posteriori adapt our results to a slightly modified scheme with respect to the choice used in this work.

O	S					
	$\sqrt{t_0}$	m_π	m_{K}	$m_{\bar{\mathrm{D}}}$	$m_{\mathrm{D_s}}$	m_{η_c}
$f_{\mathrm{D_s}}$	-1.7329	68.9924	-54.5896	25.5276	—	—
f_{D}	7.1078	4.2036	-65.2799	12.8368	—	—
$f_{\mathrm{D_s}}/f_{\mathrm{D}}$	-0.048606	0.306618	0.108713	0.049473	—	—
$f_{\mathrm{D_s}}$	-1.4314	65.0836	-55.7642	—	25.4634	—
f_{D}	7.1966	1.7997	-66.0017	—	12.7215	—
$f_{\mathrm{D_s}}/f_D$	-0.047772	0.302094	0.107553	—	0.049883	—
$f_{\mathrm{D_s}}$	-1.7556	70.6697	-55.3147	—	—	21.3979
f_{D}	6.9742	5.6292	-65.5603	—	—	10.5432
$f_{\mathrm{D_s}}/f_D$	-0.047976	0.306910	0.106676	—	—	0.042791

Table 7. Scheme dependence $S\frac{\partial O}{\partial S}$ of observable O with respect to the quantity S. In the case of f_{D} and $f_{\mathrm{D_s}}$ the units are MeV, the scheme dependence of the ratio is dimensionless. The horizontal lines divide three blocks that differ by the matching of the charm quark mass. The central values of the six quantities S are $\sqrt{t_0} = 0.1449\,\mathrm{fm}$, $m_\pi = 134.8\,\mathrm{MeV}$, $m_{\mathrm{K}} = 494.2\,\mathrm{MeV}$, $m_{\bar{\mathrm{D}}} = 1899.4\,\mathrm{MeV}$, $m_{\mathrm{D_s}} = 1966.0\,\mathrm{MeV}$, $m_{\eta_c} = 2978.0\,\mathrm{MeV}$.

References

[1] M. Bruno et al., *Simulation of QCD with $N_f = 2 + 1$ flavors of non-perturbatively improved Wilson fermions*, *JHEP* **02** (2015) 043 [`arXiv:1411.3982`] [InSPIRE].

[2] D. Mohler, S. Schaefer and J. Simeth, *CLS $2 + 1$ flavor simulations at physical light- and strange-quark masses*, *EPJ Web Conf.* **175** (2018) 02010 [`arXiv:1712.04884`] [InSPIRE].

[3] RQCD collaboration, *Scale setting and the light baryon spectrum in $N_f = 2 + 1$ QCD with Wilson fermions*, *JHEP* **05** (2023) 035 [`arXiv:2211.03744`] [InSPIRE].

[4] B. Sheikholeslami and R. Wohlert, *Improved continuum limit lattice action for QCD with Wilson fermions*, *Nucl. Phys. B* **259** (1985) 572 [InSPIRE].

[5] J. Bulava and S. Schaefer, *Improvement of $N_f = 3$ lattice QCD with Wilson fermions and tree-level improved gauge action*, *Nucl. Phys. B* **874** (2013) 188 [`arXiv:1304.7093`] [InSPIRE].

[6] M. Lüscher and P. Weisz, *On-shell improved lattice gauge theories*, *Commun. Math. Phys.* **98** (1985) 433 [*Erratum ibid.* **98** (1985) 433] [InSPIRE].

[7] M. Lüscher and S. Schaefer, *Lattice QCD without topology barriers*, *JHEP* **07** (2011) 036 [`arXiv:1105.4749`] [InSPIRE].

[8] M. Dalla Brida, T. Korzec, S. Sint and P. Vilaseca, *High precision renormalization of the flavour non-singlet Noether currents in lattice QCD with Wilson quarks*, *Eur. Phys. J. C* **79** (2019) 23 [`arXiv:1808.09236`] [InSPIRE].

[9] ALPHA collaboration, *Non-perturbative improvement of the axial current in $N_f = 3$ lattice QCD with Wilson fermions and tree-level improved gauge action*, *Nucl. Phys. B* **896** (2015) 555 [arXiv:1502.04999] [INSPIRE].

[10] RQCD collaboration, *Masses and decay constants of the η and η' mesons from lattice QCD*, *JHEP* **08** (2021) 137 [arXiv:2106.05398] [INSPIRE].

[11] ALPHA collaboration, *Hadronic physics from a Wilson fermion mixed-action approach: charm quark mass and $D_{(s)}$ meson decay constants*, *Eur. Phys. J. C* **84** (2024) 506 [arXiv:2309.14154] [INSPIRE].

[12] FERMILAB LATTICE and MILC collaborations, *B- and D-meson leptonic decay constants from four-flavor lattice QCD*, *Phys. Rev. D* **98** (2018) 074512 [arXiv:1712.09262] [INSPIRE].

[13] FLAVOUR LATTICE AVERAGING GROUP (FLAG) collaboration, *FLAG review* 2021, *Eur. Phys. J. C* **82** (2022) 869 [arXiv:2111.09849] [INSPIRE].

[14] S. Collins et al., *Leptonic decay constants for D-mesons from 3-flavour CLS ensembles*, *EPJ Web Conf.* **175** (2018) 13019 [arXiv:1711.08657] [INSPIRE].

[15] S. Collins et al., *Charmed pseudoscalar decay constants on three-flavour CLS ensembles with open boundaries*, *PoS* **LATTICE2016** (2017) 368 [arXiv:1701.05502] [INSPIRE].

[16] M. Bruno, T. Korzec and S. Schaefer, *Setting the scale for the CLS $2 + 1$ flavor ensembles*, *Phys. Rev. D* **95** (2017) 074504 [arXiv:1608.08900] [INSPIRE].

[17] RQCD collaboration, *Lattice simulations with $N_f = 2 + 1$ improved Wilson fermions at a fixed strange quark mass*, *Phys. Rev. D* **94** (2016) 074501 [arXiv:1606.09039] [INSPIRE].

[18] ALPHA collaboration, *Critical slowing down and error analysis in lattice QCD simulations*, *Nucl. Phys. B* **845** (2011) 93 [arXiv:1009.5228] [INSPIRE].

[19] M. Lüscher and S. Schaefer, *Lattice QCD with open boundary conditions and twisted-mass reweighting*, *Comput. Phys. Commun.* **184** (2013) 519 [arXiv:1206.2809] [INSPIRE].

[20] M. Lüscher and S. Schaefer, *openQCD — simulation programs for lattice QCD webpage*, http://luscher.web.cern.ch/luscher/openQCD/.

[21] M. Hasenbusch, *Speeding up the hybrid Monte Carlo algorithm for dynamical fermions*, *Phys. Lett. B* **519** (2001) 177 [hep-lat/0107019] [INSPIRE].

[22] I.P. Omelyan, I.M. Mryglod and R. Folk, *Symplectic analytically integrable decomposition algorithms: classification, derivation, and application to molecular dynamics, quantum and celestial mechanics simulations*, *Comput. Phys. Commun.* **151** (2003) 272.

[23] J.C. Sexton and D.H. Weingarten, *Hamiltonian evolution for the hybrid Monte Carlo algorithm*, *Nucl. Phys. B* **380** (1992) 665 [INSPIRE].

[24] M. Lüscher, *Deflation acceleration of lattice QCD simulations*, *JHEP* **12** (2007) 011 [arXiv:0710.5417] [INSPIRE].

[25] A. Frommer et al., *Adaptive aggregation-based domain decomposition multigrid for the lattice Wilson-Dirac operator*, *SIAM J. Sci. Comput.* **36** (2014) A1581 [arXiv:1303.1377] [INSPIRE].

[26] S. Kuberski, *Low-mode deflation for twisted-mass and RHMC reweighting in lattice QCD*, *Comput. Phys. Commun.* **300** (2024) 109173 [arXiv:2306.02385] [INSPIRE].

[27] A.D. Kennedy, I. Horváth and S. Sint, *A new exact method for dynamical fermion computations with nonlocal actions*, *Nucl. Phys. B Proc. Suppl.* **73** (1999) 834 [hep-lat/9809092] [INSPIRE].

[28] M.A. Clark and A.D. Kennedy, *Accelerating dynamical fermion computations using the rational hybrid Monte Carlo (RHMC) algorithm with multiple pseudofermion fields*, *Phys. Rev. Lett.* **98** (2007) 051601 [hep-lat/0608015] [InSPIRE].

[29] D. Mohler and S. Schaefer, *Remarks on strange-quark simulations with Wilson fermions*, *Phys. Rev. D* **102** (2020) 074506 [arXiv:2003.13359] [InSPIRE].

[30] T. Bhattacharya et al., *Improved bilinears in lattice QCD with non-degenerate quarks*, *Phys. Rev. D* **73** (2006) 034504 [hep-lat/0511014] [InSPIRE].

[31] P. Korcyl and G.S. Bali, *Non-perturbative determination of improvement coefficients using coordinate space correlators in $N_f = 2 + 1$ lattice QCD*, *Phys. Rev. D* **95** (2017) 014505 [arXiv:1607.07090] [InSPIRE].

[32] M. Lüscher, S. Sint, R. Sommer and P. Weisz, *Chiral symmetry and $O(a)$ improvement in lattice QCD*, *Nucl. Phys. B* **478** (1996) 365 [hep-lat/9605038] [InSPIRE].

[33] ALPHA collaboration, *Heavy Wilson quarks and $O(a)$ improvement: nonperturbative results for b_g*, *JHEP* **01** (2024) 188 [arXiv:2401.00216] [InSPIRE].

[34] S. Sint and R. Sommer, *The running coupling from the QCD Schrödinger functional: a one loop analysis*, *Nucl. Phys. B* **465** (1996) 71 [hep-lat/9508012] [InSPIRE].

[35] S. Güsken et al., *Nonsinglet axial vector couplings of the baryon octet in lattice QCD*, *Phys. Lett. B* **227** (1989) 266 [InSPIRE].

[36] S. Güsken, *A study of smearing techniques for hadron correlation functions*, *Nucl. Phys. B Proc. Suppl.* **17** (1990) 361 [InSPIRE].

[37] M. Falcioni, M.L. Paciello, G. Parisi and B. Taglienti, *Again on $SU(3)$ glueball mass*, *Nucl. Phys. B* **251** (1985) 624 [InSPIRE].

[38] M. Bruno and R. Sommer, *On fits to correlated and auto-correlated data*, *Comput. Phys. Commun.* **285** (2023) 108643 [arXiv:2209.14188] [InSPIRE].

[39] ALPHA collaboration, *Monte Carlo errors with less errors*, *Comput. Phys. Commun.* **156** (2004) 143 [*Erratum ibid.* **176** (2007) 383] [hep-lat/0306017] [InSPIRE].

[40] A. Ramos, *Automatic differentiation for error analysis of Monte Carlo data*, *Comput. Phys. Commun.* **238** (2019) 19 [arXiv:1809.01289] [InSPIRE].

[41] F. Joswig, S. Kuberski, J.T. Kuhlmann and J. Neuendorf, *pyerrors: a python framework for error analysis of Monte Carlo data*, *Comput. Phys. Commun.* **288** (2023) 108750 [arXiv:2209.14371] [InSPIRE].

[42] G. Colangelo, A. Fuhrer and S. Lanz, *Finite volume effects for nucleon and heavy meson masses*, *Phys. Rev. D* **82** (2010) 034506 [arXiv:1005.1485] [InSPIRE].

[43] M. Lüscher, *Properties and uses of the Wilson flow in lattice QCD*, *JHEP* **08** (2010) 071 [*Erratum ibid.* **03** (2014) 092] [arXiv:1006.4518] [InSPIRE].

[44] FLAVOUR LATTICE AVERAGING GROUP (FLAG) collaboration, *Review of lattice results concerning low-energy particle physics*, *Eur. Phys. J. C* **77** (2017) 112 [arXiv:1607.00299] [InSPIRE].

[45] HPQCD collaboration, *Precise determination of decay rates for $\eta_c \to \gamma\gamma$, $J/\psi \to \gamma\eta_c$, and $J/\psi \to \eta_c e^+ e^-$ from lattice QCD*, *Phys. Rev. D* **108** (2023) 014513 [arXiv:2305.06231] [InSPIRE].

[46] HPQCD collaboration, *Charmonium properties from lattice QCD+QED: hyperfine splitting, J/ψ leptonic width, charm quark mass, and a_μ^c*, *Phys. Rev. D* **102** (2020) 054511 [arXiv:2005.01845] [INSPIRE].

[47] PARTICLE DATA GROUP collaboration, *Review of particle physics*, *PTEP* **2022** (2022) 083C01 [INSPIRE].

[48] G.S. Bali, S. Collins and C. Ehmann, *Charmonium spectroscopy and mixing with light quark and open charm states from $n_F = 2$ lattice QCD*, *Phys. Rev. D* **84** (2011) 094506 [arXiv:1110.2381] [INSPIRE].

[49] L. Levkova and C. DeTar, *Charm annihilation effects on the hyperfine splitting in charmonium*, *Phys. Rev. D* **83** (2011) 074504 [arXiv:1012.1837] [INSPIRE].

[50] QCD-TARO collaboration, *Contribution of disconnected diagrams to the hyperfine splitting of charmonium*, *JHEP* **08** (2004) 004 [hep-lat/0404016] [INSPIRE].

[51] G.S. Bali, S. Collins, A. Cox and A. Schäfer, *Masses and decay constants of the $D_{s0}^*(2317)$ and $D_{s1}(2460)$ from $N_f = 2$ lattice QCD close to the physical point*, *Phys. Rev. D* **96** (2017) 074501 [arXiv:1706.01247] [INSPIRE].

[52] J.L. Goity and C.P. Jayalath, *Strong and electromagnetic mass splittings in heavy mesons*, *Phys. Lett. B* **650** (2007) 22 [hep-ph/0701245] [INSPIRE].

[53] ALPHA collaboration, *Determination of the charm quark mass in lattice QCD with $2 + 1$ flavours on fine lattices*, *JHEP* **05** (2021) 288 [arXiv:2101.02694] [INSPIRE].

[54] P. Virtanen et al., *SciPy 1.0 — fundamental algorithms for scientific computing in python*, *Nature Meth.* **17** (2020) 261 [arXiv:1907.10121] [INSPIRE].

[55] J.J. Moré, *The Levenberg-Marquardt algorithm: implementation and theory*, in *Numerical analysis*, G.A. Watson ed., Springer, Berlin, Heidelberg, Germany (1978), p. 105 [DOI:10.1007/BFb0067700].

[56] J.L. Goity, *Chiral perturbation theory for SU(3) breaking in heavy meson systems*, *Phys. Rev. D* **46** (1992) 3929 [hep-ph/9206230] [INSPIRE].

[57] O. Bär and M. Golterman, *Chiral perturbation theory for gradient flow observables*, *Phys. Rev. D* **89** (2014) 034505 [*Erratum ibid.* **89** (2014) 099905] [arXiv:1312.4999] [INSPIRE].

[58] K. Symanzik, *Continuum limit and improved action in lattice theories. 1. Principles and ϕ^4 theory*, *Nucl. Phys. B* **226** (1983) 187 [INSPIRE].

[59] K. Symanzik, *Continuum limit and improved action in lattice theories. 2. $O(N)$ nonlinear sigma model in perturbation theory*, *Nucl. Phys. B* **226** (1983) 205 [INSPIRE].

[60] N. Husung, P. Marquard and R. Sommer, *Asymptotic behavior of cutoff effects in Yang-Mills theory and in Wilson's lattice QCD*, *Eur. Phys. J. C* **80** (2020) 200 [arXiv:1912.08498] [INSPIRE].

[61] N. Husung, P. Marquard and R. Sommer, *The asymptotic approach to the continuum of lattice QCD spectral observables*, *Phys. Lett. B* **829** (2022) 137069 [arXiv:2111.02347] [INSPIRE].

[62] N. Husung, *SymEFT predictions for local fermion bilinears*, *PoS* **LATTICE2023** (2024) 364 [arXiv:2401.04303] [INSPIRE].

[63] H. Akaike, *A new look at the statistical model identification*, *IEEE Trans. Automatic Control* **19** (1974) 716 [INSPIRE].

[64] H. Akaike, *Information theory and an extension of the maximum likelihood principle*, in *Springer series in statistics*, Springer Science+Business Media, New York, NY, U.S.A. (1998), p. 199 [DOI:10.1007/978-1-4612-1694-0_15] [INSPIRE].

[65] W.I. Jay and E.T. Neil, *Bayesian model averaging for analysis of lattice field theory results*, *Phys. Rev. D* **103** (2021) 114502 [arXiv:2008.01069] [INSPIRE].

[66] S. Weinberg, *Effective gauge theories*, *Phys. Lett. B* **91** (1980) 51 [INSPIRE].

[67] M. Nobes, *Efficient simulation of heavy quark vacuum polarization*, hep-lat/0501009 [INSPIRE].

[68] FERMILAB LATTICE and MILC collaborations, $B^0_{(s)}$-*mixing matrix elements from lattice QCD for the Standard Model and beyond*, *Phys. Rev. D* **93** (2016) 113016 [arXiv:1602.03560] [INSPIRE].

[69] ALPHA collaboration, *QCD coupling from a nonperturbative determination of the three-flavor* Λ *parameter*, *Phys. Rev. Lett.* **119** (2017) 102001 [arXiv:1706.03821] [INSPIRE].

[70] ALPHA collaboration, *Light quark masses in* $N_f = 2 + 1$ *lattice QCD with Wilson fermions*, *Eur. Phys. J. C* **80** (2020) 169 [arXiv:1911.08025] [INSPIRE].

[71] RQCD collaboration, *Octet baryon isovector charges from* $N_f = 2 + 1$ *lattice QCD*, *Phys. Rev. D* **108** (2023) 034512 [arXiv:2305.04717] [INSPIRE].

[72] S. Cali et al., *Charm sea effects on charmonium decay constants and heavy meson masses*, *Eur. Phys. J. C* **81** (2021) 733 [arXiv:2105.12278] [INSPIRE].

[73] W. Lucha, D. Melikhov and S. Simula, *Isospin breaking in the decay constants of heavy mesons from QCD sum rules*, *Phys. Lett. B* **765** (2017) 365 [arXiv:1609.05050] [INSPIRE].

[74] A. Desiderio et al., *First lattice calculation of radiative leptonic decay rates of pseudoscalar mesons*, *Phys. Rev. D* **103** (2021) 014502 [arXiv:2006.05358] [INSPIRE].

[75] D. Giusti et al., *Methods for high-precision determinations of radiative-leptonic decay form factors using lattice QCD*, *Phys. Rev. D* **107** (2023) 074507 [arXiv:2302.01298] [INSPIRE].

[76] HPQCD collaboration, *Update: precision* D_s *decay constant from full lattice QCD using very fine lattices*, *Phys. Rev. D* **82** (2010) 114504 [arXiv:1008.4018] [INSPIRE].

[77] FERMILAB LATTICE and MILC collaborations, *B- and D-meson decay constants from three-flavor lattice QCD*, *Phys. Rev. D* **85** (2012) 114506 [arXiv:1112.3051] [INSPIRE].

[78] HPQCD collaboration, $|V_{cd}|$ *from D meson leptonic decays*, *Phys. Rev. D* **86** (2012) 054510 [arXiv:1206.4936] [INSPIRE].

[79] χQCD collaboration, *Charm and strange quark masses and* f_{D_s} *from overlap fermions*, *Phys. Rev. D* **92** (2015) 034517 [arXiv:1410.3343] [INSPIRE].

[80] RBC/UKQCD collaboration, *The decay constants* f_D *and* f_{D_s} *in the continuum limit of* $N_f = 2 + 1$ *domain wall lattice QCD*, *JHEP* **12** (2017) 008 [arXiv:1701.02644] [INSPIRE].

[81] RBC/UKQCD collaboration, $SU(3)$-*breaking ratios for* $D_{(s)}$ *and* $B_{(s)}$ *mesons*, arXiv:1812.08791 [INSPIRE].

[82] ETM collaboration, *Leptonic decay constants* f_K, f_D, *and* f_{D_s} *with* $N_f = 2 + 1 + 1$ *twisted-mass lattice QCD*, *Phys. Rev. D* **91** (2015) 054507 [arXiv:1411.7908] [INSPIRE].

[83] PACS-CS collaboration, *Charm quark system at the physical point of* $2 + 1$ *flavor lattice QCD*, *Phys. Rev. D* **84** (2011) 074505 [arXiv:1104.4600] [INSPIRE].

[84] χQCD collaboration, *Charmed and* ϕ *meson decay constants from* $2 + 1$-*flavor lattice QCD*, *Chin. Phys. C* **45** (2021) 023109 [arXiv:2008.05208] [INSPIRE].

[85] P. Dimopoulos, R. Frezzotti, M. Garofalo and S. Simula, *K- and $D_{(s)}$-meson leptonic decay constants with physical light, strange and charm quarks by ETMC*, *PoS* **LATTICE2021** (2021) 472 [arXiv:2110.01294] [INSPIRE].

[86] ALPHA collaboration, *Scale setting for $N_f = 3 + 1$ QCD*, *Eur. Phys. J. C* **80** (2020) 349 [arXiv:2002.02866] [INSPIRE].

[87] D. Krause, *JUWELS: modular tier-0/1 supercomputer at the Jülich supercomputing centre*, *JLSRF* **5** (2019) A135 [INSPIRE].

[88] D. Krause and P. Thörnig, *JURECA: modular supercomputer at Jülich supercomputing centre*, *JLSRF* **4** (2018) A132.

[89] H. Baier et al., *QPACE: a QCD parallel computer based on Cell processors*, *PoS* **LAT2009** (2009) 001 [arXiv:0911.2174] [INSPIRE].

[90] Y. Nakamura et al., *Lattice QCD applications on QPACE*, arXiv:1103.1363 [INSPIRE].

[91] SciDAC et al. collaborations, *The chroma software system for lattice QCD*, *Nucl. Phys. B Proc. Suppl.* **140** (2005) 832 [hep-lat/0409003] [INSPIRE].

[92] S. Heybrock, M. Rottmann, P. Georg and T. Wettig, *Adaptive algebraic multigrid on SIMD architectures*, *PoS* **LATTICE2015** (2016) 036 [arXiv:1512.04506] [INSPIRE].

[93] T. Korzec, *Calculate meson correlators with openQCD GitHub webpage*, https://github.com/to-ko/mesons.

[94] C.R. Harris et al., *Array programming with NumPy*, *Nature* **585** (2020) 357 [arXiv:2006.10256] [INSPIRE].

[95] D. Maclaurin, D. Duvenaud and R.P. Adams, *Autograd: effortless gradients in Numpy*, in *ICML* 2015 *AutoML workshop*, volume 238, https://indico.ijclab.in2p3.fr/event/2914/contributions/6483/subcontributions/180/attachments/6060/7185/automl-short.pdf, (2015), p. 5.

[96] J.D. Hunter, *Matplotlib: a 2D graphics environment*, *Comput. Sci. Eng.* **9** (2007) 90 [INSPIRE].